INDEX COPERNICUS INTERNATIONAL

Bio-Algorithms and Med-Systems

WWW.BAMSJOURNAL.COM ISSN: 1896-530X

ORIGINAL ARTICLE

Received: 10.12.2025
Accepted: 04.03.2026
Published: 22.04.2026

CITE THIS ARTICLE AS:
Kacprzak K, Beyene E, Choiński J, Chug N, Curceanu C, Czerwiński E, et al. "Methodology for time and TOT calibration of a modular J-PET scanner with prompt gamma emitters ^{22}Na and ^{44}Sc," Bio-Algorithms and Med-Systems vol. 22, no. 1, pp. 36-55, 2026, DOI: 10.5604/01.3001.0055.6703

AUTHORS' CONTRIBUTION:
A – Conceptualization
B – Data Curation
C – Formal Analysis
D – Funding Acquisition
E – Investigation
F – Methodology
G – Project Administration
H – Resources
I – Software
J – Supervision
K – Validation
L – Visualization
M – Writing – Original Draft
N – Writing – Review & Editing

CORRESPONDING AUTHOR:
Krzysztof Kacprzak; Faculty of Physics, Astronomy and Applied Computer Science, Jagiellonian University; S. Łojasiewicza 11 street, 30-348 Kraków, Poland; E-mail: k.kacprzak@alumni.uj.edu.pl

Methodology for time and TOT calibration of a modular J-PET scanner with prompt gamma emitters ^{22}Na and ^{44}Sc

Krzysztof Kacprzak[1,2ABCEFIKLMN], Ermias Beyene[1,2,3EN], Jarosław Choiński[4EN], Neha Chug[1,2EN], Catalina Curceanu[5EN], Eryk Czerwiński[1,2BEN], Manish Das[1,2,3EN], Jakub Hajduga[6EN], Sharareh Jalali[1,2,3EN], Tevfik Kaplanoglu[1,2,3EN], Łukasz Kapłon[1,2EN], Kamila Kasperska[1,2,3EN], Aleksander Khreptak[1,2EN], Grzegorz Korcyl[1,2EIN], Tomasz Kozik[1,2EN], Karol Kubat[1,2EN], Sumit Kumar Kundu[1,2EN], Deepak Kumar[1,2,3EN], Edward Lisowski[7EN], Filip Lisowski[7EN], Justyna Mędrala-Sowa[1,2,3EN], Simbarashe Moyo[1,2,3EN], Wiktor Mryka[1,2,3EN], Szymon Niedźwiecki[1,2EN], Anand Pandey[1,2EN], Piyush Pandey[1,2,3EN], Szymon Parzych[1,2,3EN], Alessio Porcelli[1,2,5,8 EHN], Bartłomiej Rachwał[6EN], Martin Rädler[1,2EN], Sushil Sharma[1,2EHN], Magdalena Skurzok[1,2EN], Anna Stolarz[4EN], Tomasz Szumlak[6EHN], Pooja Tanty[1,2,3EN], Keyvan Tayefi Ardebili[1,2,3EN], Satyam Tiwari[1,2,3EN], Anoop Venadan[1,2EN], Ewa Łucja Stępień[1,2DEGHJN], Paweł Moskal[1,2ABDEFGHJKN]

[1]Faculty of Physics, Astronomy and Applied Computer Science, Jagiellonian University, Kraków, Poland
[2]Center for Theranostics, Jagiellonian University, Kraków, Poland
[3]Jagiellonian University, Doctoral School of Exact and Natural Sciences, Kraków, Poland
[4]Heavy Ion Laboratory, University of Warsaw, Warsaw, Poland
[5]INFN, Laboratori Nazionali di Frascati, Frascati, Italy
[6]AGH University of Kraków, Kraków, Poland
[7]Cracow University of Technology, Faculty of Mechanical Engineering, Kraków, Poland
[8]Center of Astronomical Research, Technology, Education, and Outreach, University of Antofagasta, Antofagasta, Chile

ABSTRACT

Objective: The goal of the work is to develop a set of methods for calibrating the positron emission tomography system built from plastic scintillators, and to present the results of the modular J-PET scanner time of flight (TOF) and time over threshold (TOT) synchronisation.

Methods: Measurements with radionuclide ^{22}Na and ^{44}Sc (used as a point-like source and enclosed in a collimator) were performed using the modular J-PET scanner, which detects signals from annihilation photons and prompt gamma. The data were gathered with a trigger-less data acquisition system and analysed with a dedicated software framework. The detection modules were synchronised with the procedures, correcting time offsets and normalising TOT measurements.

Results: The application of the time calibration methods yields a fully synchronised detector that is capable of producing the image of the source. TOF resolution for modular J-PET is determined to be about 490 ps (FWHM).

Conclusions: The J-PET scanner, built from plastic scintillators, can be calibrated using $\beta^+\gamma$ emitters and taking advantage of the fact that the direction of propagation of annihilation and prompt photons are not correlated.

KEYWORDS

positron emission tomography, modular J-PET, sodium, scandium, medical imaging

LIST OF ABBREVIATIONS

AFOV – axial field-of-view
CRT – coincidence resolving time
DAQ – data acquisition system
FEE – front-end electronics
FPGA – field-programmable gate array
FPGAs – field-programmable gate arrays
FWHM – full width at half maximum
GATE – Geant4 Application for Tomographic Emission
J-PET – Jagiellonian positron emission tomography
PET – positron emission tomography
RPRC – Radiopharmaceuticals Research and Production Center
SiPM – silicon photomultiplier
SiPMs – silicon photomultipliers
TB-PET – total body PET
TB-J-PET – total body Jagiellonian PET
TDC – time-to-digital converter
TOF – time of flight
TOT – time over threshold

BRIEF DESCRIPTION OF THE WORK

This article describes the methods applied to calibrate a prototype Jagiellonian positron emission tomography (J-PET) modular detector constructed of plastic scintillator strips. The set of methods enable the synchronisation of time offsets of various elements of the detector and the relative normalisation of the measured value of time over threshold (TOT). The methods are validated using data collected from measurements with the radioactive sources ^{22}Na and ^{44}Sc; their execution and results are described and discussed. As an example of the performance of a calibrated scanner, the image of the source is reconstructed and the time of flight (TOF) distribution is determined based on the selection of back-to-back 511 keV photons from the point-like source, placed in the centre of the detector.

INTRODUCTION

The J-PET group is developing a low-cost total body Jagiellonian PET (TB-J-PET) [1, 2]. The TB-J-PET systems have rapidly developed recently [3], with currently available uExplorer [4], PennPET Explorer [5], Siemens Biograph Vision Quadra [6] and United Imaging Panorama GS [7]. However, the presently available systems are expensive due to the price of crystal scintillators, which prevents their broad application in clinical practice. Therefore, it is important to develop methods that would enable the low-cost construction of such systems. The major factor in lowering the price is the use of scintillators made of plastic, which is a solution proposed by a J-PET group.

As a first step on the way to develop the low-cost TB-J-PET scanner, the modular J-PET detector was constructed. It is a lightweight and portable apparatus with 50-cm axial field-of-view (AFOV) consisting of 24 axially arranged modules built from plastic scintillator strips [8]. Since its commissioning it has been deployed in several sites in various configurations: in the National Center of Hadron Radiotherapy in Cracow [9], the Medical University of Warsaw [10] and the University Hospital in Cracow [11]. The modular J-PET is a multiphoton scanner capable of positronium [10, 12, 13] and quantum entanglement imaging [14, 15]. The fundamental physics experiments are conducted predominantly with ^{22}Na isotope [14, 16, 17], while for positronium imaging the ^{44}Sc was identified as the best radionuclide [1, 18].

Calibrating the setup is a necessary preparation for every PET device. Establishing the calibration procedures for J-PET is the goal of the presented work. In commercial PETs, constructed of crystal scintillators, it is required to calibrate energy registration by photodetectors, recognising the photo peak and thus the interactions of 511 keV photons. In J-PET, made of plastic scintillators, we do not register energy directly; we rely on TOT measurements as an estimate of energy deposited via the Compton effect.

The construction of the modular J-PET detector is described in more detail in section *Modular J-PET*. The dedicated software was created for data reconstruction, selection and analysis as part of the development of this prototype; it is described in section *Analysis software*. The detector's sensitivity and spatial resolution were assessed in separate works [19, 20]. The methods of data acquisition, signal reconstruction and time, and TOT calibration as well as methods of data selection are described thoroughly in sections *Data acquisition, reconstruction and calibration* and *Selection of annihilation events*. The article concludes with a discussion of the obtained results, and the challenges and prospects for further development.

MATERIALS AND METHODS

This section includes the description of the device that is being calibrated, the piece of software used for the analysis and the radionuclides used in the experiment, and it describes the measurements performed.

Modular J-PET

The J-PET introduces plastic scintillators as material for constructing a large FOV PET [1, 21]. Technology was deployed and tested

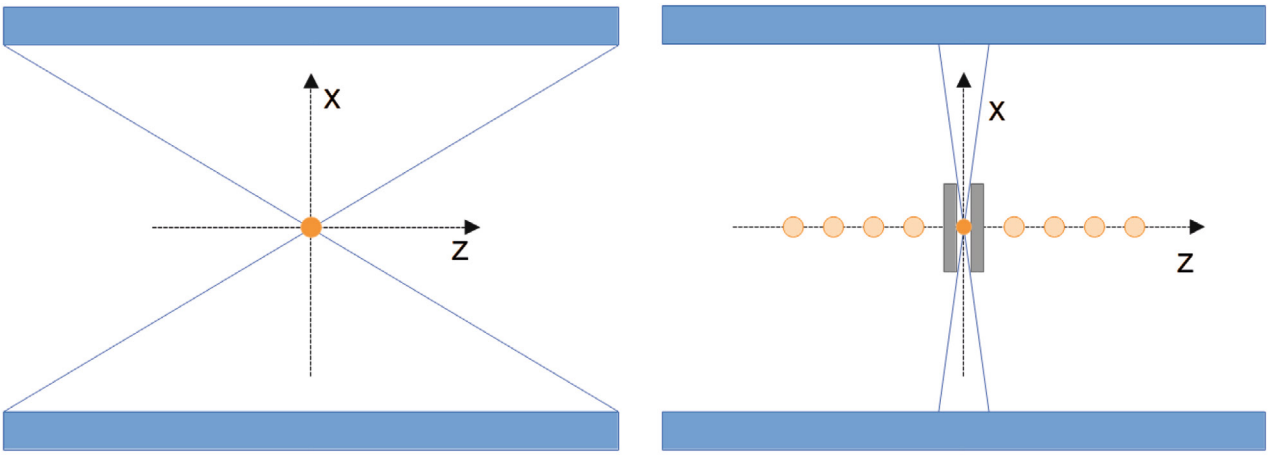

Fig. 1. Diagrams of measurements performed with ^{22}Na: on the left the point-like source, emitting photons in all directions and irradiating the full length of the scintillators. This kind of measurement was done with sodium and scandium sources; on the right, the sodium source inside the collimator with photons reaching only part of the scintillator strips. The circles mark the positions of the source, in the centre and also in various placements along the *z*-axis.

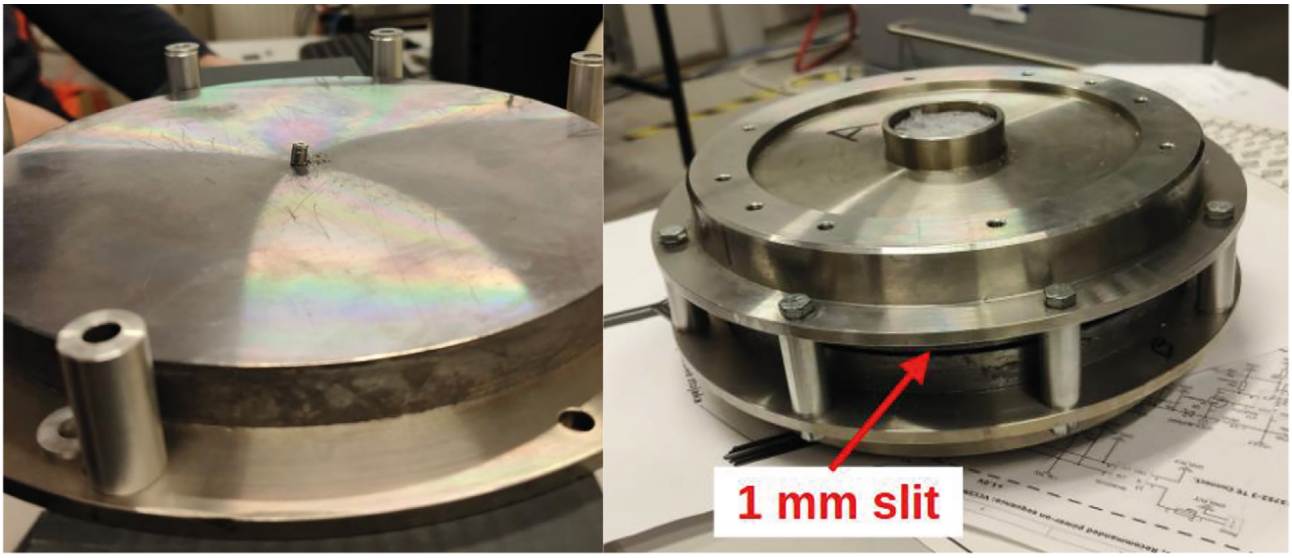

Fig. 2. Photos of the collimator plates (left) before closing, with the sodium source placed in the centre; (right) the closed casing with the 1-mm slit.

in numerous cases; the one described in this paper consists of 24 modules; each has 13 BC-404 rectangular plastic scintillators [22]. A single strip has dimensions of 50 cm × 2.4 cm × 0.6 cm. Rows of four silicon photomultipliers (SiPM) are attached to the ends of every strip, receiving the light that propagates through the scintillator and reaches the edges. The signals are registered on two thresholds on each SiPM, giving a total of 4,992 acquisition channels. A trigger-less readout chain starts with front-end electronics (FEE) and field-programmable gate arrays (FPGAs) based on time-to-digital converter (TDC) readout boards [23–25]. The data are streamed to the concentrator boards, Xilinx VCU108 platforms equipped with SFP FMC addons to accommodate 12 links to the FEE, one link to the central controller and one 10GbE data output to storage. The central controller is a Xilinx ZCU102 ZynqMPSoC platform, which is the source of the master clock and synchronisation pulse, which are distributed through the concentrators to the FEE.

Analysis software

The calibration and signal reconstruction procedures described in the following sections were prepared and executed with the J-PET analysis framework, which is a platform for data analysis developed within the J-PET group. It is a dynamic C++ library using CERN ROOT as its base, depending on the BOOST libraries. This environment allows the processing of data from the modular detector in HLD (binary) format and saves the result in ROOT files as ntuples. The analysis is divided into steps that together create a chain of tasks in which the output of one constitutes the input for the following. At each point in the chain we can investigate the data with control histograms.

The J-PET Analysis Framework allows for flexible usage of calibration files in ASCII, JSON or ROOT format at any step in the workflow. Also, any type of selection parameters or conditions

can be applied in the signal reconstruction, giving a possibility to prepare samples of events for various purposes, i.e., fundamental physics studies [14, 16, 17] or medical imaging [10, 26]. The output of the selection can be converted into list-mode files, which serve as the input for image reconstruction programs such as CaSTOR [27]. It also handles Monte Carlo generated data, prepared with typical environments such as Geant4 [28] or Geant4 Application for Tomographic Emission (GATE) [29].

Calibration measurements

The following measurements were performed in January and February 2025 in order to prepare the calibrations:

1. The point-like source of ^{22}Na, 5.88 MBq activity, placed inside a plexiglass rod, was positioned in the geometrical centre of the detector for 6 hours (see Fig. 1., 3.).
2. ^{22}Na in collimator – the same source was enclosed between two metal plates (Fig. 1.–3.). The slit size was 1 mm. The collimated source was placed in 13 positions along the *z*-axis, from –12 to 12 cm, with an interval of 2 cm, each time measured for 1 hour. Additionally, a long measurement of 12 hours was taken for the 0 cm position.
3. ^{44}Sc linear source, 140 cm long. The radionuclide was dissolved in 11 mL of water, and a tube was filled with the solution and placed in the centre of the detector along the *z*-axis. The activity at the beginning of the measurement was 7.51 MBq and the data acquisition lasted 20 minutes. The isotope ^{44}Sc for the purposes of calibration of the detector and measurements of the positronium decay, using nuclear reaction ^{44}Ca(p, n)^{44}Sc, was produced at the Radiopharmaceuticals Research and Production Center (RPRC), which is part of the Heavy Ion Laboratory of the University of Warsaw [30, 31]. The targets used in the production of the ^{44}Sc were made of natural $CaCO_3$. The target material, 89 mg of calcium carbonate, compacted into a pellet with a 6-mm diameter, was placed in a graphite shell with a diameter of 10 mm. Such construction of the target improves the dissipation of the heat deposited by the beam. One can find target preparation details in [32, 33]. After irradiation the targets were transported to the J-PET scanner.

DATA ACQUISITION, RECONSTRUCTION AND CALIBRATION

The calibration procedures are focused on the synchronisation of timing information and normalisation of the response of SiPM across the detector. The process is divided into steps, as shown in Fig. 4.

Each part of the process has some calibration constants that are applied at the current step. The values of time offsets or normalisation parameters are found in the subsequent task, so it is necessary to start the procedure again until the next, uncalibrated step. The

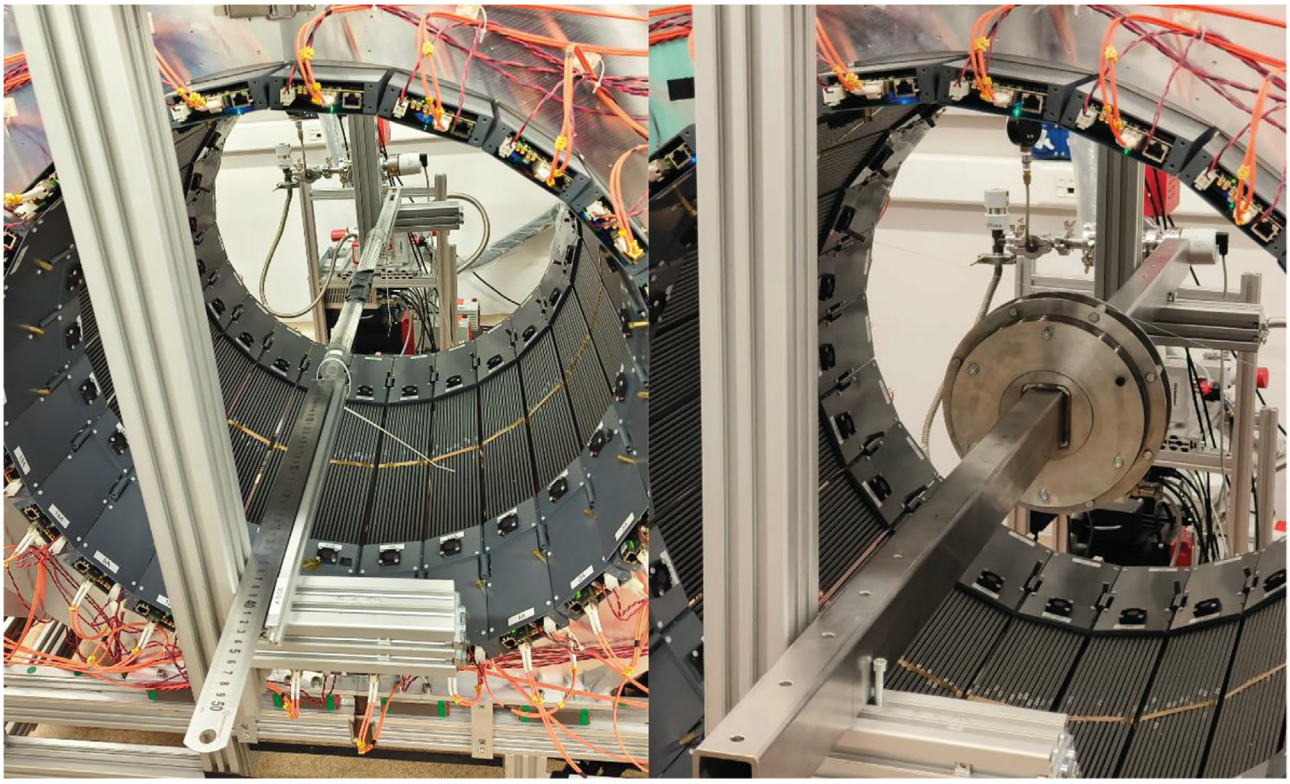

Fig. 3. Photos of the data-taking phases: (left), the point-like source inside a plexiglass rod; (right) the measurement with the same source placed between two collimator plates.

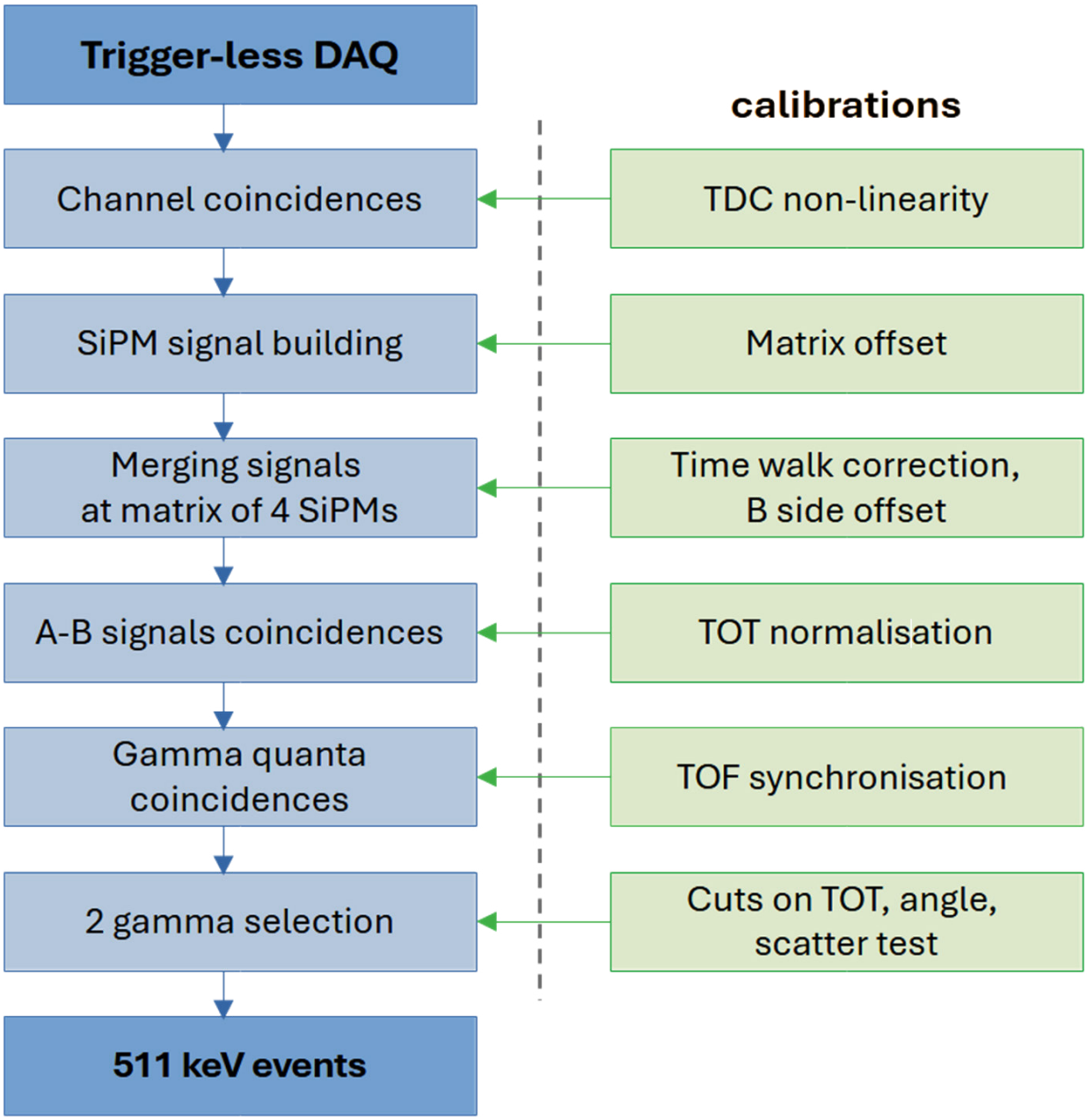

Fig. 4. A diagram illustrating the order of the subsequent tasks, procedures performed on acquired data and the accompanying calibrations that were applied during the signal reconstruction. Any step can be calibrated once or repeatedly in order to obtain the optimal values of the constants.

synchronisation of TOF and time-walk corrections is iterated several times; the time offsets are changed in all the elements at once until we find the values that yield the best result of TOF possible. The details of all the calibrations are described further in the text.

DAQ and TDC nonlinearity correction

Signals are read out by SiPM on two thresholds, set to 30 and 70 mV above the baseline. Each strip is connected to 4 SiPMs at both sides, so in total the data acquisition system (DAQ) consists of 4,992 channels. The digitising and readout is based on FPGAs, and the arrival time measured by the TDC with a high resolution time of 12 ps [24, 34]. The response of the converter is not perfectly linear, as shown in Fig. 5. This nonlinear effect is compensated for with TDC calibration: for each measured fine time we calculate the discrepancy of converter response and a linear function. This number is then subtracted from the fine time of the registered timestamp.

Filtering of the repeated edges

The procedure of signal building, described in the next section, matches the coincident leading and trailing signals on the same channel. Before this algorithm was applied we attempted to clean the sample of any suspected noise generated by SiPMs. The amount of the noise depended on the setting of the readout

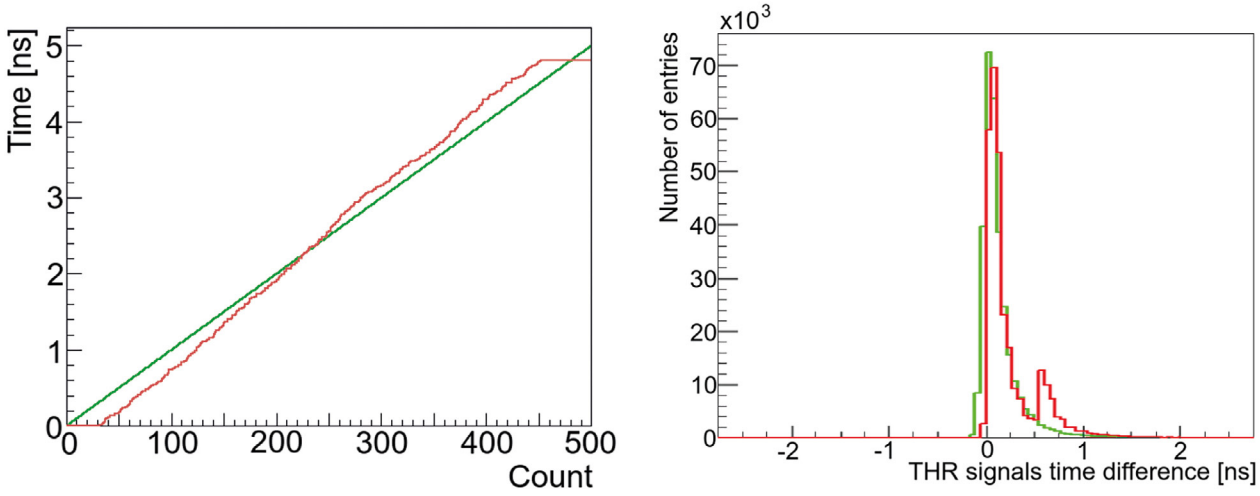

Fig. 5. Two plots showing the concept of calibrating TDC nonlinearity. On the left plot: the green line marks the expected conversion from the clock counter to the time domain, while the red the measured, real response. The difference between the two lines is a calibration constant later used in the proper calculation of the fine time of the registered timestamp. In the histogram on the right side we can see the distributions of the time difference $t_{LEAD}^{THR2} - t_{LEAD}^{THR1}$ between leading edges of the same signal registered on two thresholds (Fig. 7.). The red line shows data before correcting for nonlinearity, and an additional, smaller peak is visible, which is absent on the green spectrum calculated with calibrated data.

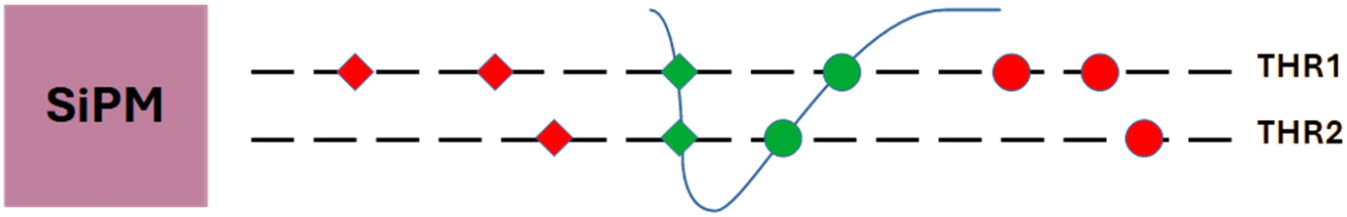

Fig. 6. Scheme of a two-channel SiPM registering timestamps of leading and trailing edges of the signals (marked with diamond and circle points, respectively). At times more timestamps appear in data sets that do not match the opposite type of the consecutive one. The reconstruction of the signals is based on matching pairs of leading-trailing edges, so these repeated types of edges are rejected by the filter. In the diagram the accepted timestamps are marked in green and the rejected ones in red.

threshold level above the baseline. It manifested as random, with additional registered leading/trailing edges, not following the expected sequence. The scheme presented in Fig. 6. explains the applied selection. Application of this filtering rejected 3.5% of channel signals when the two thresholds at SiPMs were set for 30 and 70 mV above the baseline.

SiPM signal building

Trigger-less DAQ produces a series of timestamps assigned to specific channels. The next step after the filtration is to combine this information into a signal registered by a photomultiplier. Each SiPM probes incoming signals at two channels with a different threshold setting. The algorithm reconstructing the signals compares the time and type of edge of the consecutive channel readouts and pairs leading-trailing timestamps from the same channel, if $(t^{TRAIL} - t^{LEAD}) < 200$ ns. In the next step we compare LEAD times from the created pairs from both thresholds and match them if $(t^{LEAD}_{THR2} - t^{LEAD}_{THR1}) < 15$ ns. Further on, we use t^{LEAD}_{THR1} as the registration time of the signal. To estimate the charge carried out by the signal, we use the TOT method, which is calculated in the following way:

$$TOT_{SiPM} = (t^{TRAIL}_{THR1} - t^{LEAD}_{THR1}) \cdot (THR1 - BASELINE) + (t^{TRAIL}_{THR2} - t^{LEAD}_{THR2}) \cdot (THR2 - THR1) \quad (1)$$

For the purpose of calibration, only signals with pairs on both thresholds are saved for further analysis to reduce the contribution of low TOT noise. The timestamps that did not fulfill the given conditions and were not paired with others are rejected. In the case of calibration measurements, the percentage of cut timestamps is 0.015%.

Matrix signals building and synchronisation

The previous part described how signals on each SiPM are created. These photomultipliers are attached using optical gel to plastic scintillators in a 1 × 4 matrix (Fig. 8.) at both ends of every strip. Now we want to synchronise the readouts of all 4 to correctly match the incoming signals.

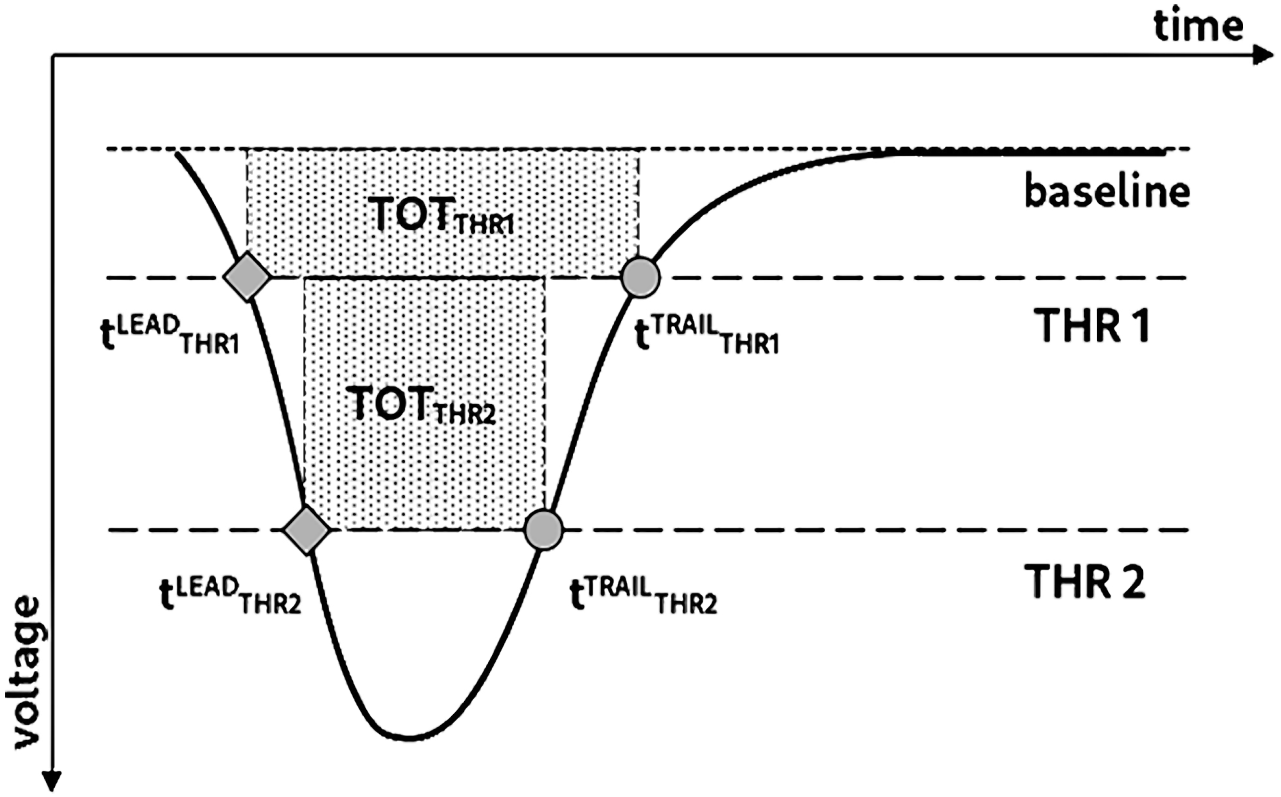

Fig. 7. Scheme of a signal curve, which is registered by a single SiPM. In this idealised case the signal is registered when the ascending voltage crosses two thresholds (marked with two squares) and again when descending (circles), thus causing the readout of 4 timestamps. The arrival time is simplified to be equal to one registered on the leading edge and the lower threshold. Furthermore, the energy carried by the signal can be estimated as TOT. The area above the signal curve is estimated as a sum of the fields of two rectangles, according to the equation (1).

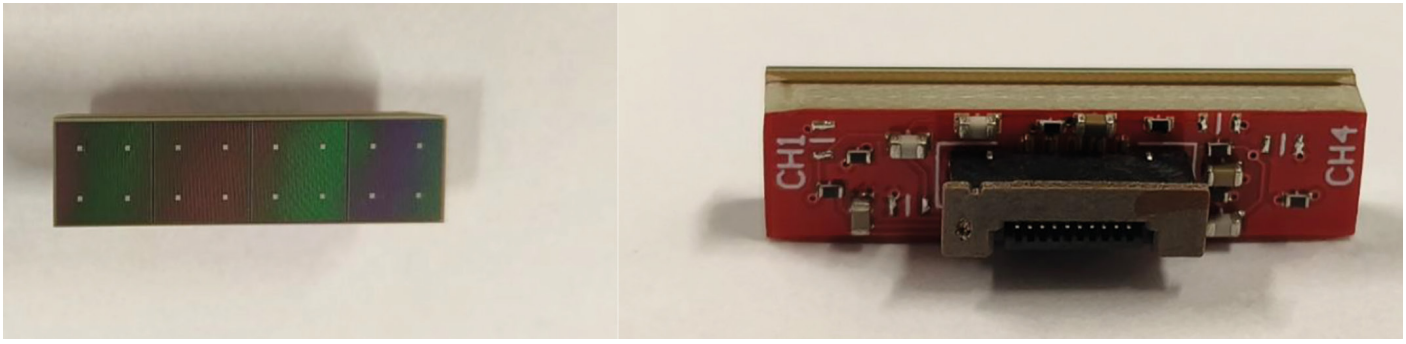

Fig. 8. Front and back of a matrix of 4 SiPMs.

If SiPM signals that registration times are coinciding in the time window of 5 ns, it is assumed that they originate from the same interaction of the gamma ray in the strip and are merged into one "matrix signal". The average value of registration time $t_{SIG\_A,B}$ and average TOT is calculated. Fig. 9. shows how several signals are arriving at the SiPMs in a time window. The reconstructed time of arrival of signals on SiPMs 2, 3 and 4 is modified by an offset. It is calculated in reference to the time reconstructed by SiPM 1, threshold 1. The timestamps found on threshold 2 are modified by the same offset as corresponding threshold 1. After synchronisation, the selection of the coincidence time window is set to 3.5 ns.

Reconstruction of the gamma ray interaction in the strip

The reconstruction of the position and time of gamma ray interactions in the scintillators follows the scheme described previously in Ref. [35]. Precise estimation is necessary for building lines-of-response and then creating the image of the source.

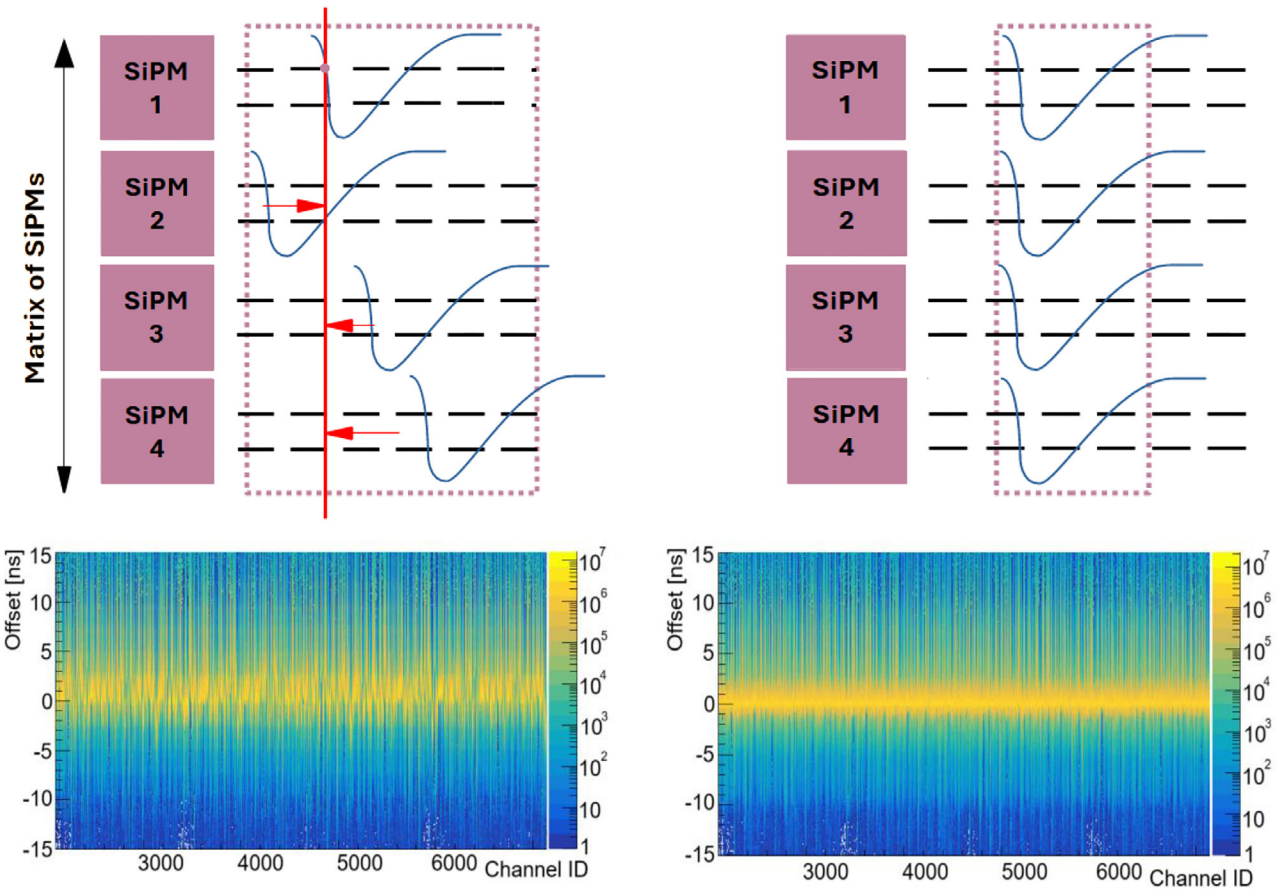

Fig. 9. The images in the upper row show the concept of synchronisation of SiPM readouts of the same matrix, as explained in the text. The lower row shows the histogram of time differences calculated for each channel and the reference channels. The left shows the result before application of the offsets, and the right afterward.

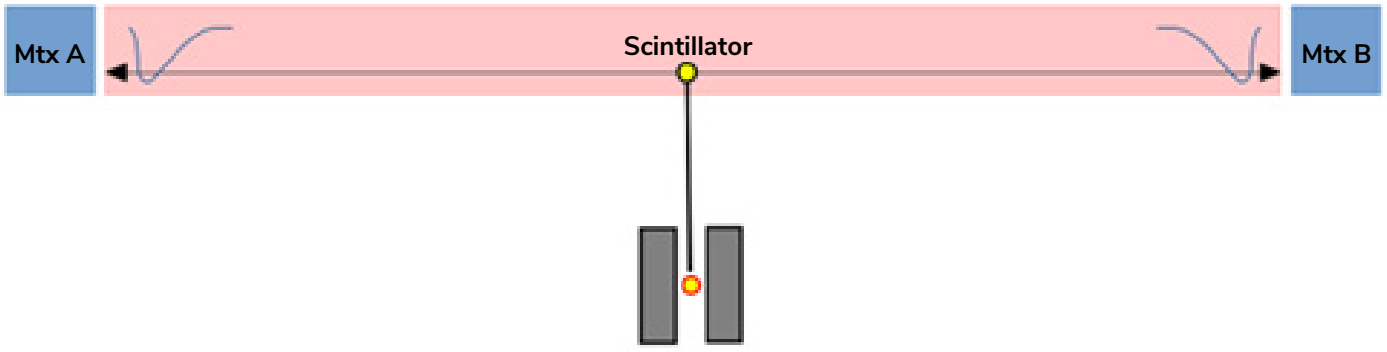

Fig. 10. Schematic of the propagation of the light in the plastic scintillator, originating from the interaction point of the gamma ray with the material. The light reaches matrices of SiPMs (A, B), which register it as a signal.

If two signals registered by the matrices of SiPMs on the opposite sides of the same strip coincide in time (window of 4 ns), then we construct a hit with the following characteristics:

$$t_{HIT} = (t_{SIG\_A} + t_{SIG\_B})/2 \quad (2)$$

$$t_{DIFF} = t_{SIG\_B} - t_{SIG\_A} \quad (3)$$

$$z_{POS} = v_{EFF} \cdot t_{DIFF} / 2 \quad (4)$$

where t_{HIT} is a reconstructed hit time, $t_{SIG\_A,B}$ are the arrival times of the signals registered on the opposite sites of the scintillator, z_{POS} is the position of the reconstructed interaction along the strip measuring from the centre of the strip and v_{EFF} is the effective velocity of light in the scintillator. The values of v_{EFF} for each strip are found using the method described in section *Estimation of effective velocity of light*. As for the X and Y coordinates of the hit, we assume the geometrical centre in XY of the strip that we have registered an interaction with (Fig. 10.).

A–B sides synchronisation

Each measurement of the interaction time has some equipment offset that needs to be compensated for if we want to compare the registration time of the hits in different strips and calculate the z_{POS} correctly (Fig. 11.). To do this we analyse the data from the measurement with the point-like source, which was put in the centre of the detector. The synchronisation procedure finds correction constants δ_{STRIP}, which are subtracted from the time of the signal on one side, marked as 'B':

$$t_B^{SYNC} = t_B - \delta_{STRIP} \quad (5)$$

where δ_{STRIP} has a different value for each scintillator (Fig. 12.).

Estimation of effective velocity of light

The precise reconstruction of the position of the interactions of gamma ray in the scintillators is crucial for the construction of LORs for tomographic images. The position along the z-axis depends

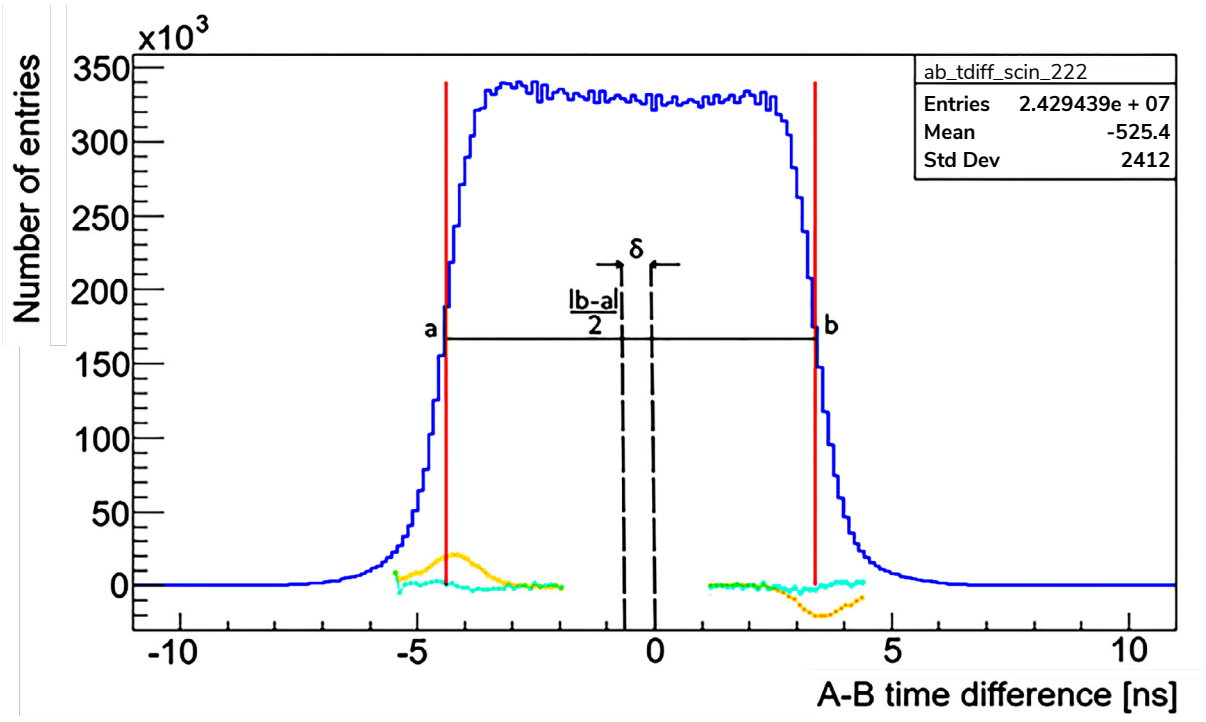

Fig. 11. Histogram of the time difference between signals registered on the opposite sides of the same strip in a measurement with a point-like source (blue line). We assume that almost the full length of the strip is irradiated uniformly and find the edges of the distribution by calculating the second derivative of the border and estimating the inflection point. The two borders are marked with red vertical lines and letters 'a' and 'b'. Yellow and teal lines show the plots of the first and second derivatives of the selected regions. Half of the distance b–a is a value of the correction δ, which has to be subtracted from the signal's time on side B to synchronise the timing of the hits.

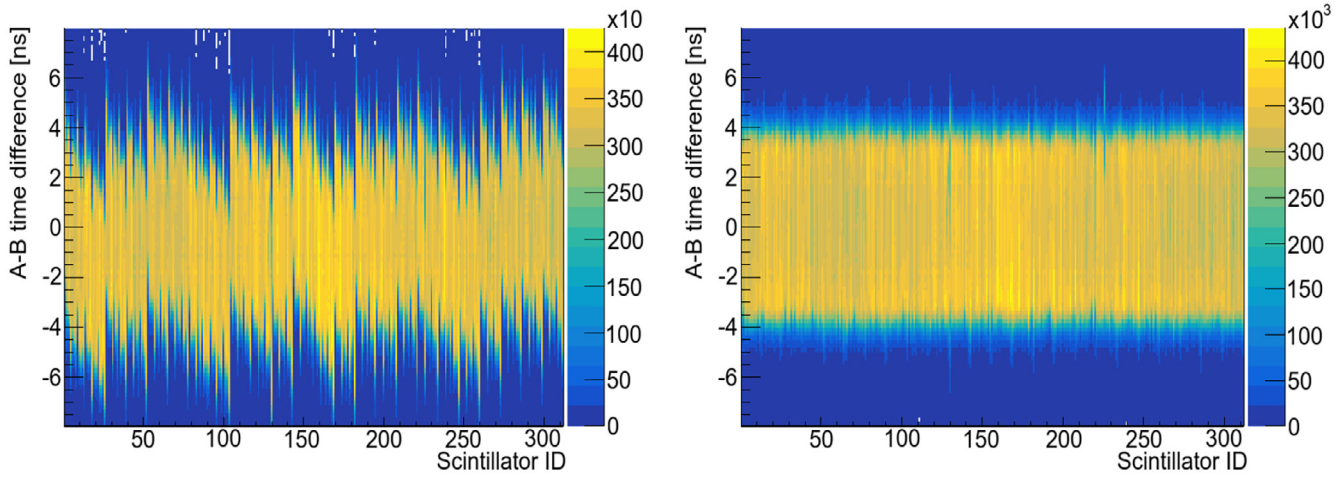

Fig. 12. Collection of histograms of the A–B time difference (same as in the example in Fig. 11) for all the scintillators, marked by ID number. The left panel shows the state before calibration, while the right panel the same data with applied corrections δ_{STRIP}, according to the equation (5).

on the value of the effective velocity of light, which is different for each plastic strip. The estimation of this parameter can be done in several ways. The simplest is to analyse the measurements done with the collimated source placed in several positions, as described in section *Calibration measurements*, then plot the time difference of hits (Eq. 3) and the maximum of the distribution versus the nominal placement of the collimator. This dependence $z_{POS}(t_{DIFF})$ for one of the scintillators is shown in Fig. 13., left. According to Equation 4, the fit parameter a is equal to $v_{EFF}/2$. This procedure is repeated for each strip (Fig. 13., right). The average value is marked by the red line and is equal to $v^{AVG}_{EFF} = 12.13 \pm 0.02$ cm/ns.

If we have only a measurement with the point-like source we can use a different approach. We can obtain the effective velocity by calculating:

$$v_{EFF} = d_{EFF} / t^{AB}_{MAX} \quad (6)$$

$$t^{AB}_{MAX} = |edge_B - edge_A| / 2 \quad (7)$$

where edge A and B are the limits found in the distribution shown in Fig. 11. The length d_{EFF} is the effective length of the scintillator that registers photon interactions. In the ideal case this d_{EFF} would be 50 cm, but as we observe in Fig. 11., the rate of hits drops near the edges, causing this length to be less than 50 cm. The values of d_{EFF} cannot be calculated directly; they also depend on the time resolution. This can be done by performing a series of assumptions about the value of d_{EFF}, reconstructing the positions of hits for the measurements with the collimator and comparing them with its nominal placement. The average value is $d^{AVG}_{EFF} = 45.08 \pm 0.06$ cm (Fig. 14.).

From this analysis we can conclude that in case of the calibration with the point-like source for the modular J-PET with 50-cm length, if t^{AB}_{MAX} is calculated (as shown in Fig. 11.) by taking time at the inflection point, $d^{AVG}_{EFF} = 45.08$ cm should be used. However, it

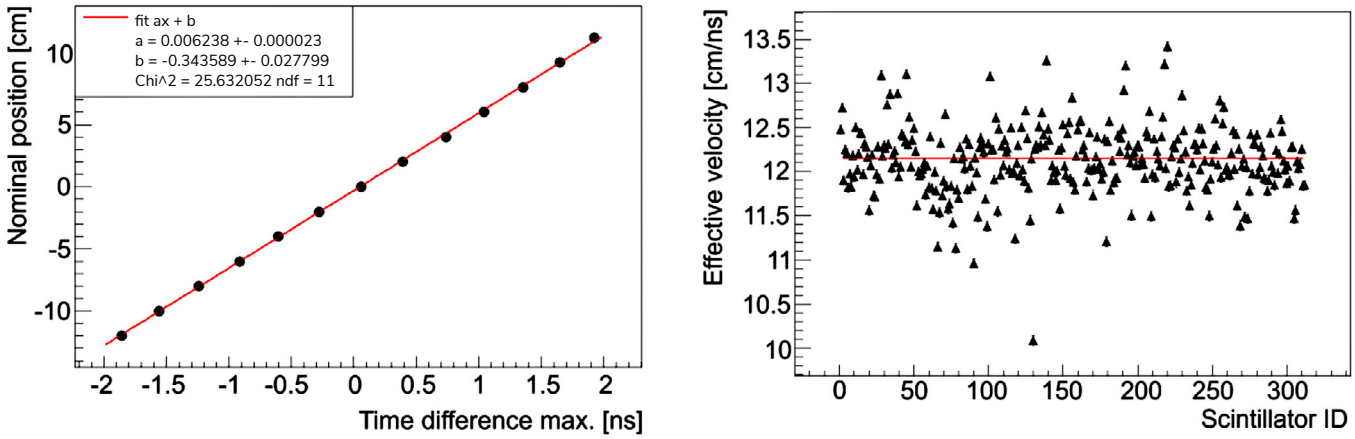

Fig. 13. The left panel presents an example of the time difference vs. the nominal position of the collimator graph for the scintillators. The linear fit reveals the value of the effective velocity, $v_{EFF} = 2a$. The right panel shows the estimation of the effective velocity of light for each scintillator.

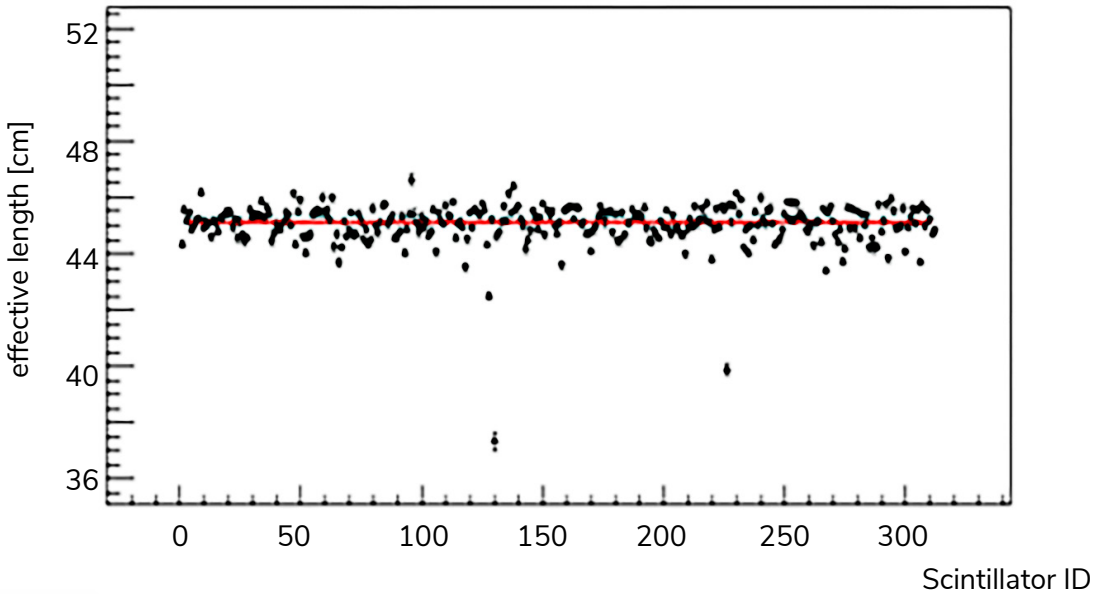

Fig. 14. Estimation of the effective length for each strip.

must be stressed that d^{AVG}_{EFF} depends on the time resolution and the geometrical setting of the source with respect to the scintillator strip.

TOT relative normalisation with ^{22}Na and ^{44}Sc sources

TOT is used to estimate the area under the curve of the signal (Eq. 1), which in turn is a measure of deposited energy; the relation between the two has been investigated in previous work [36]. What is important from the perspective of analyses and calibrations is that based on this value we can select events of a certain energy deposition range using the same criterion for all scintillator strips [35].

In a detector that measures mainly Compton scattering, it is crucial to have a unified response from all the SiPMs. The results of the measurements depend on many variables, such as temperature, which we cannot control precisely. We introduce effective corrections to the readout of each photomultiplier to normalise its response. It is done by analysing the spectra for each strip, finding the equivalents of Compton edges for annihilation photons and prompt gamma. This allows for a linear scaling of the histogram so that both edges are placed on the values, which are calculated as the averages of the found edges for annihilation photons (A) and prompt gamma (P). After obtaining the scaling factors the value of TOT for each interaction (hit) is recalculated in the following way:

$$TOT_{HIT}^{NORM} = \alpha\, TOT_{HIT} + \beta \quad (8)$$

$$\alpha = (N^P - N^A)/(E^P - E^A) \quad (9)$$

$$\beta = N^A - [(N^P - N^A) \cdot E^A / (E^P - E^A)] \quad (10)$$

where $N^{A,P}$ are nominal edges, $E^{A,P}$ are values of the inflection points of annihilation and prompt edges, respectively, found for each strip (Fig. 15., left).

Various isotopes are being used for PET imaging [1], and the question arises whether they can be utilised for calibration procedures. The ^{22}Na was selected for its stability over time, with a half-life of 2.6 years. ^{44}Sc has a significantly shorter half-life (4 h) and is not convenient for long measurements, as in the case of 12 h acquisition of data from the source in the collimator. Despite this disadvantage we can obtain clear TOT spectra with ^{44}Sc after 20 minutes and use them to perform the normalisation. Scandium was used here, as it is the most suitable radionuclide for developing positronium imaging [1, 13]. Fig. 15. presents the comparison of TOT for ^{22}Na and ^{44}Sc, showing that both can be used for this part of the calibrations. The effect of relative normalisation with both isotopes is shown in Fig. 16.

TOF synchronisation

The method of timing synchronisation was briefly described in reference [37] and is applied here. The goal of this step is to achieve the best resolution of TOF possible. This calibration requires us to distinguish between two types of gamma rays with different energies, but coming from the same position, from the same point-like source in the centre of the detector. Single annihilation photons of 511 keV and a prompt gamma of 1275 keV for ^{22}Na are identified by TOT selection, as shown in right panel of Fig. 17.

Two spectra of time differences are plotted for each strip *n*: (annihilation$_n$ – prompt$_m$) and (prompt$_n$ – annihilation$_m$), where *m* is the index of any other strip in the detector. The distance between the peaks of the distributions, δt, is found (Fig. 18.). The objective of the synchronisation is to reduce δt as much as possible by applying the correction constant, and the procedure is repeated until the spectra are aligned (lower right panel in Fig. 19.).

Found offsets are then used in the hit time reconstruction, and we can observe the final effect by plotting the value of TOF for each pair of scintillators:

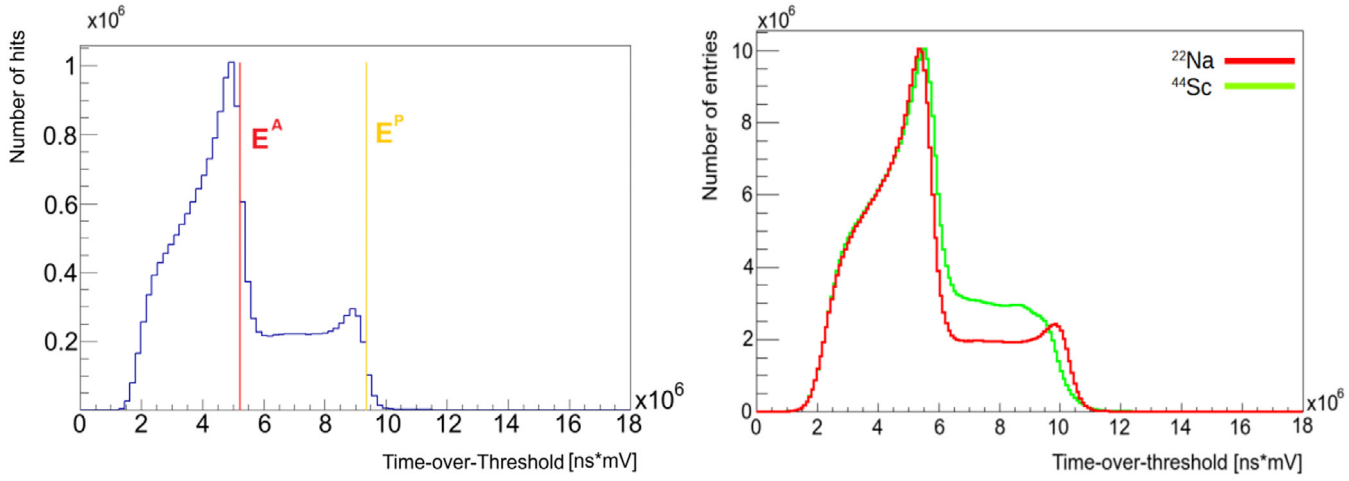

Fig. 15. Relative normalisation of TOT measurement starts with finding the equivalent of the Compton edges. For this purpose, for the selected regions around local maxima on the histogram, the first and second derivatives are calculated and the inflection points are determined. Left side: The example of TOT spectrum measured for a single plastic strip using ^{22}Na source before normalisation, with indicated inflection points E^A and E^P. The first point is treated as an annihilation edge (vertical red line), while the second is the prompt edge (yellow line). The right panel shows scaled distributions of TOT produced with ^{22}Na (red line) and ^{44}Sc (green line) after normalisation.

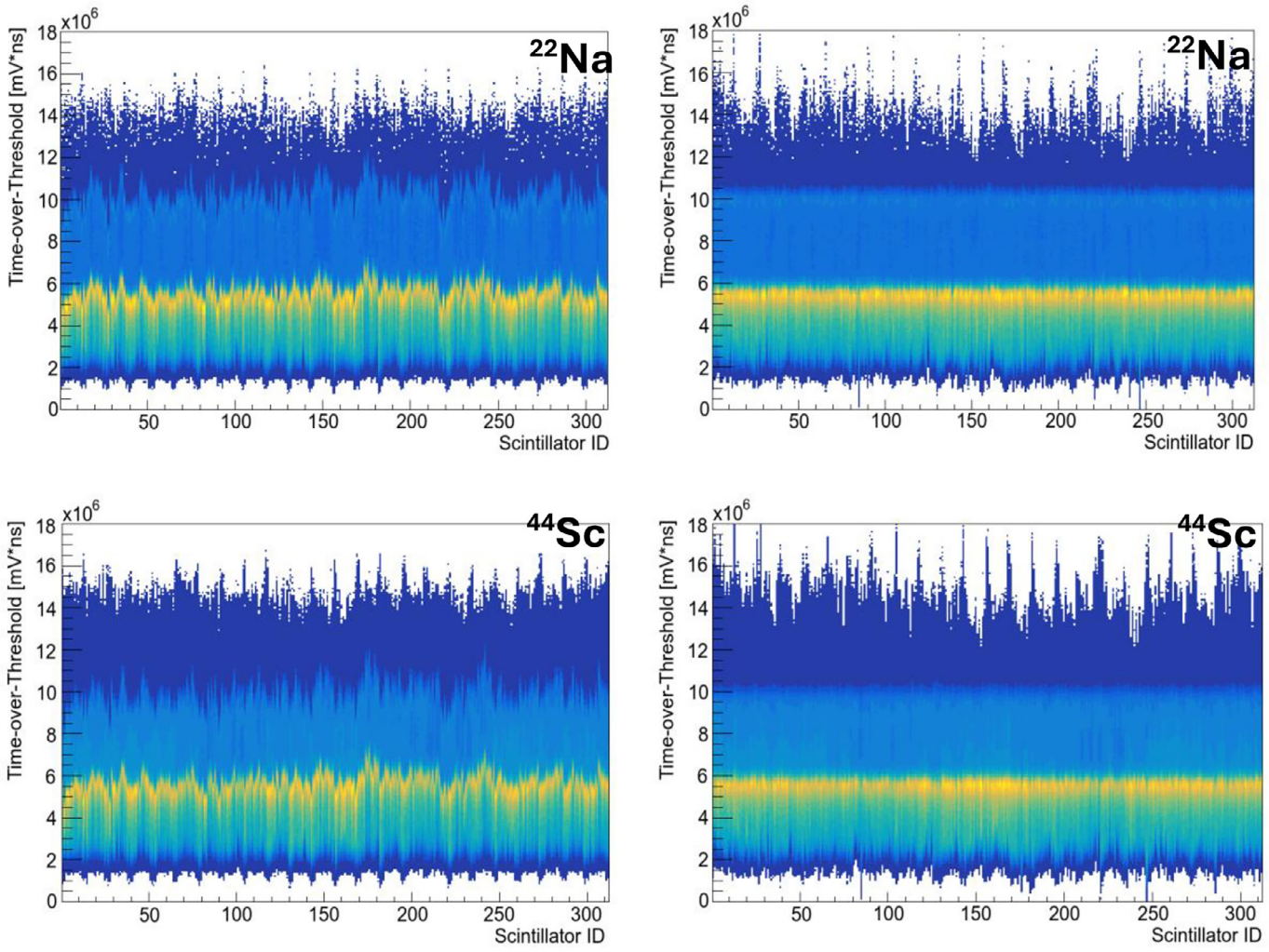

Fig. 16. Relative normalisation of TOT measurement of gamma ray interactions in plastic scintillators through the Compton effect with ^{22}Na (upper row) and ^{44}Sc (lower row) sources. For each of 312 strips, hits are reconstructed, as described in the text, and the TOT value is calculated as defined in Equation 1 and shown in Fig. 7. The spectra for all strips are collected in the form of a 2D histogram, showing the state before (left column) and after the normalisation (right column). As a result, Compton edges are situated at the same value, and it is easier to perform more exact event selection.

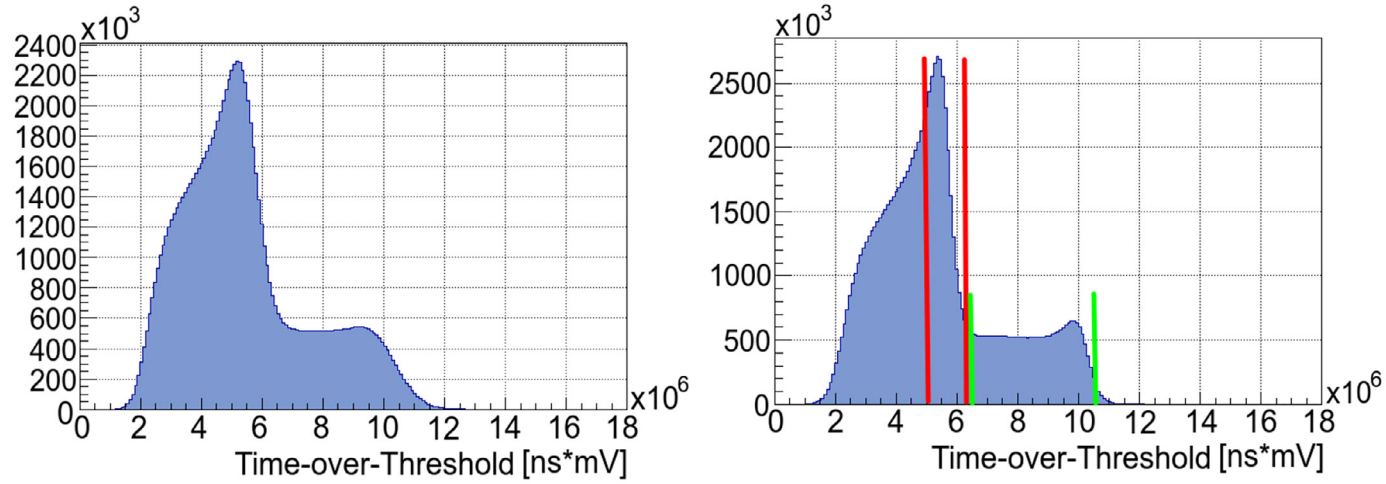

Fig. 17. The control TOT histograms for all the scintillators before (left) and after (right) calibration with the ^{22}Na source. The regions for selection of 511 keV annihilation photons (red lines) and 1275 keV prompt photons (green lines) are marked in the spectrum on the right.

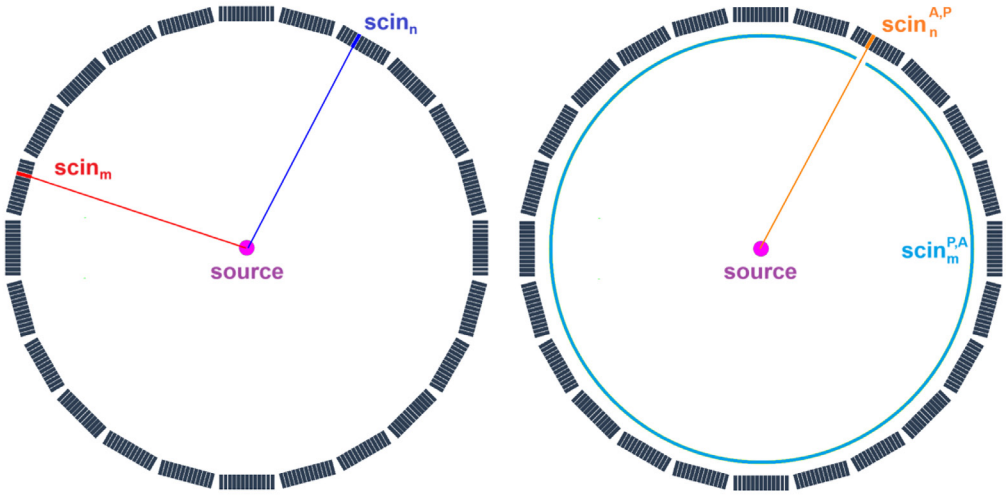

Fig. 18. Scheme showing the selection of the events for synchronisation of the reconstructed times of photon interactions in the strips. We are looking for two photons, one of which was classified as prompt (marked with blue colour in the left diagram) and the other as annihilation (red colour) based on the TOT selection (see text). For any $scin_n$ we plot two histograms with distributions of time difference: prompt gamma (P) and annihilation photon (A), in any other strip $scin_m$; annihilation photon (A) and prompt gamma (P), in any other strip $scin_m$. This way we obtain the plots on Fig. 19.: $t_{PA} = t(scin^P_n) - t(scin^A_m)$ and $t_{AP} = t(scin^A_n) - t(scin^P_m)$, where $scin^{A,P}_n$ and $scin^{PA}_m$ are the strips registering annihilation photon or prompt gamma.

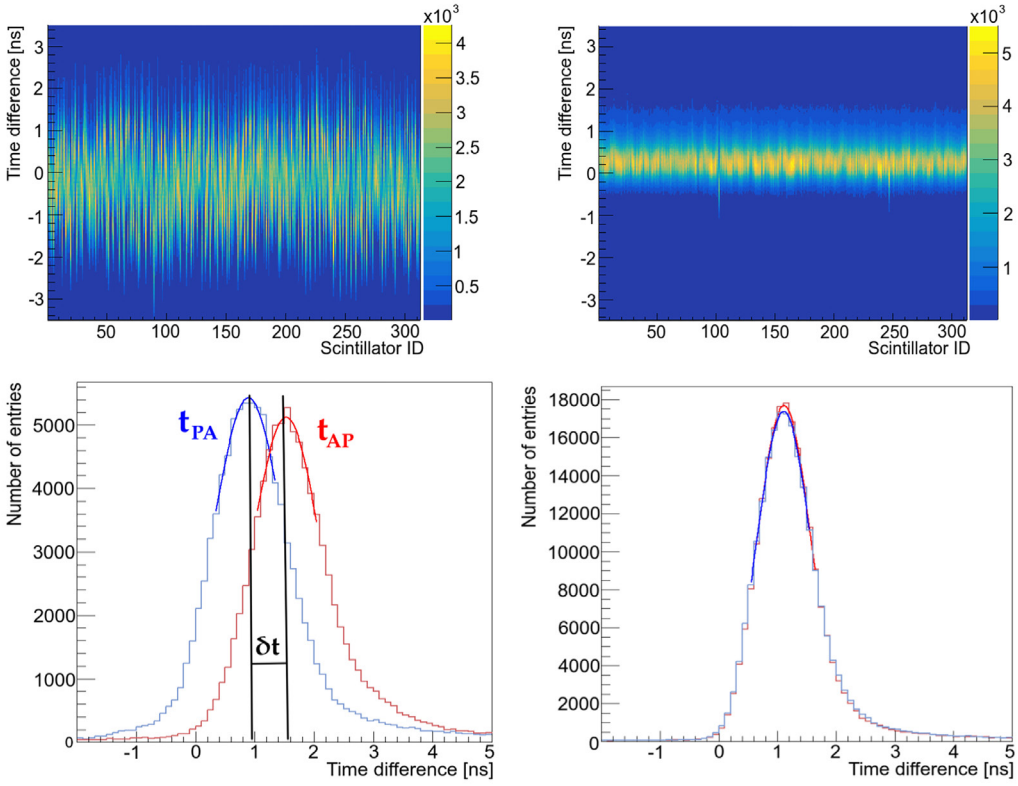

Fig. 19. Procedure of synchronisation of the TOF based on the selected events (as described in the text). Left column – before calibration, the right – after 12 iterations of the calibration procedure (Fig. 20.). The upper row shows the collection of the spectra t_{AP} (time of annihilation photon minus time of prompt gamma) for all the strips, and the lower presents both distributions, t_{AP} and t_{PA} as an example for one chosen strip.

$$TOF = t_{HIT}{}^{i} - t_{HIT}{}^{j} \quad (11)$$

where *i*, *j* indices are the IDs of the scintillators. This time difference is calculated according to the convention that the time of a hit in the strip *j* is subtracted from the time of a hit in strip *i* and *i* < *j*. The description of the selection of pairs of hits for TOF calculation is described in section *Selection of annihilation events*. Time of hit registration is corrected by a constant δt_k, found for each strip *k*:

$$t_{HIT}{}^{k} = t^{REG}{}_{HIT}{}^{k} - \delta t_k/2 \quad (12)$$

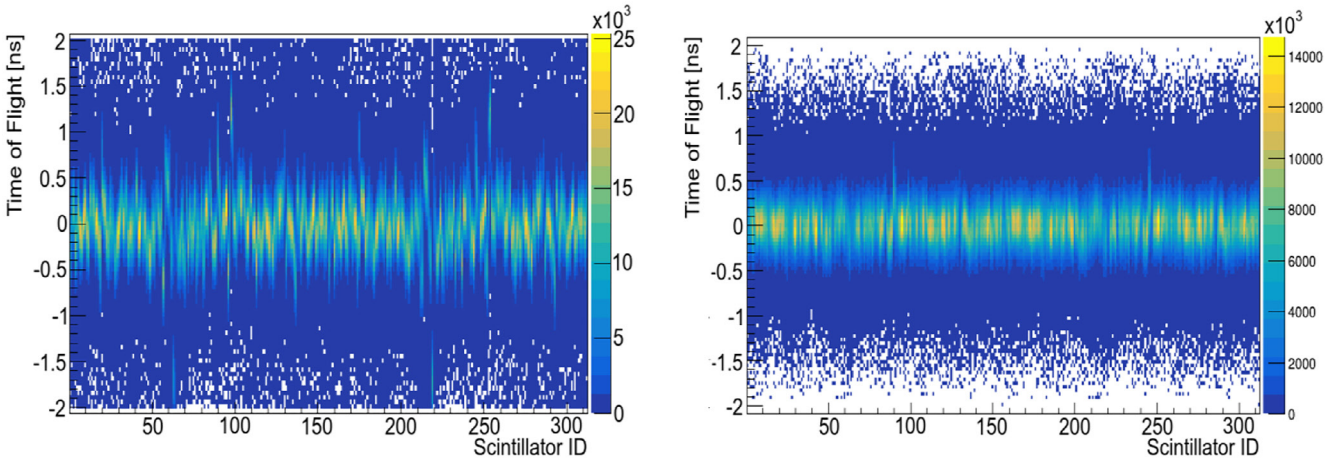

Fig. 20. Spectra of average TOF that each strip has with every other in the detector. Synchronisation of hit time performed as described in the text allows the distributions to be centred around 0 for all the scintillating strips. In the left panel – before calibration, on the right – after 12 iterations of calibration.

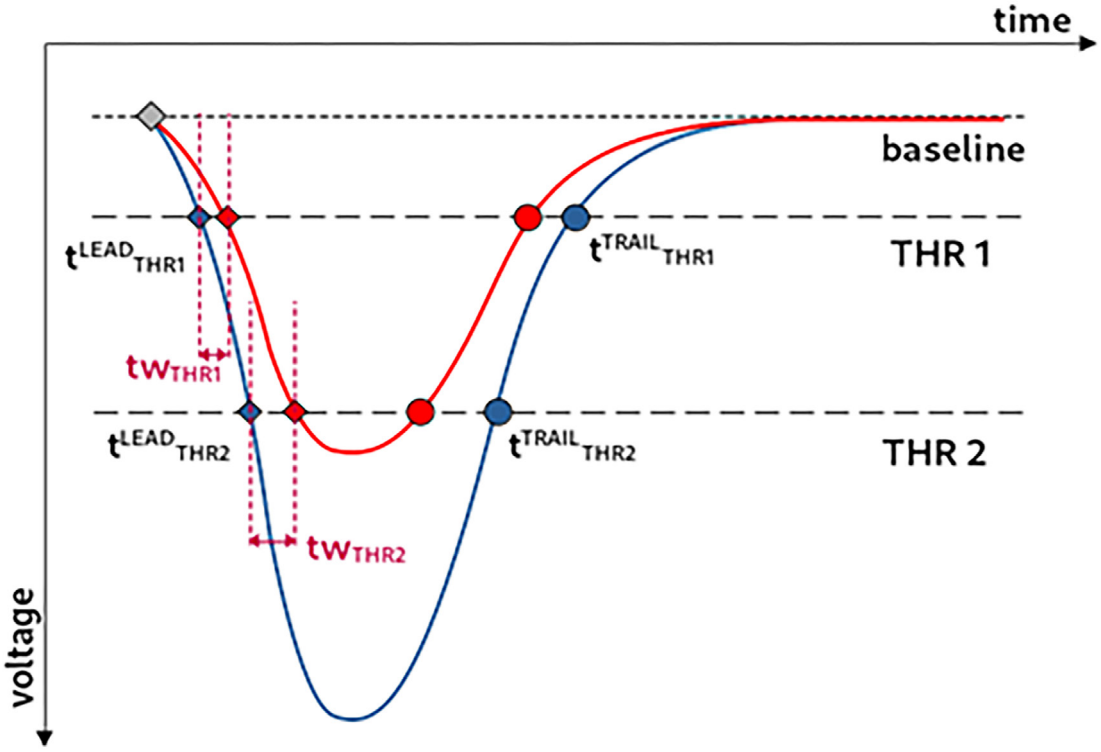

Fig. 21. Scheme showing the cause of the time walk effect in signal readout on two thresholds.

Time walk effect correction

The time walk effect is due to the difference between the real beginning of the signal and the time of registration. which varies depending on the shape and the threshold. The rise time of the signal is constantly independent of its amplitude, which leads to different gradients of the leading edge and therefore different trigger times for a fixed threshold. The example in Fig. 21. shows that two signals with the same arrival time (grey square where blue and red lines meet the baseline) are registered on the first (lower) threshold with a different result. The signal with a smaller TOT (red curve) will be registered later than the signal with a bigger TOT (blue line). This delay becomes bigger at the higher threshold, THR2. Estimating the dependence of the time walk effect from TOT will allow us to correct the time of the reconstructed signals and improve the time resolution of the device.

The measurement with the collimated source in the geometrical centre of the detector allows us to register photon interactions in the middle of the strips ($z = 0$). This way the signals are arriving

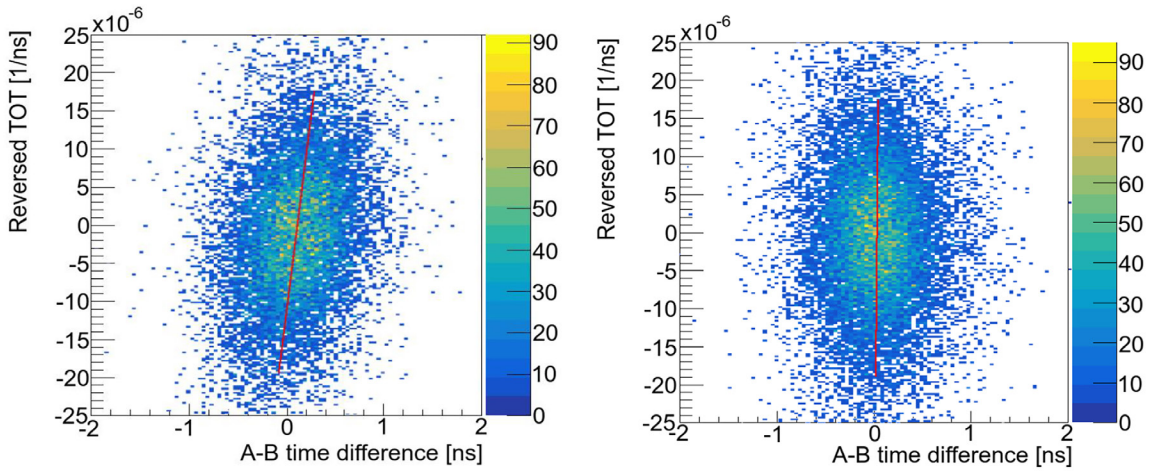

Fig. 22. Example of histograms for one strip showing reversed TOT as a function of A–B time difference for registered photon interactions in a measurement with the collimated source placed at $z = 0$. The red line indicates a fit to the maximum projections of reversed TOT in 10 intervals. The inclination of this line is the value of the parameter α. The left panel shows the result before, with the right panel after walk correction and the red line visibly rotated and aligned vertically.

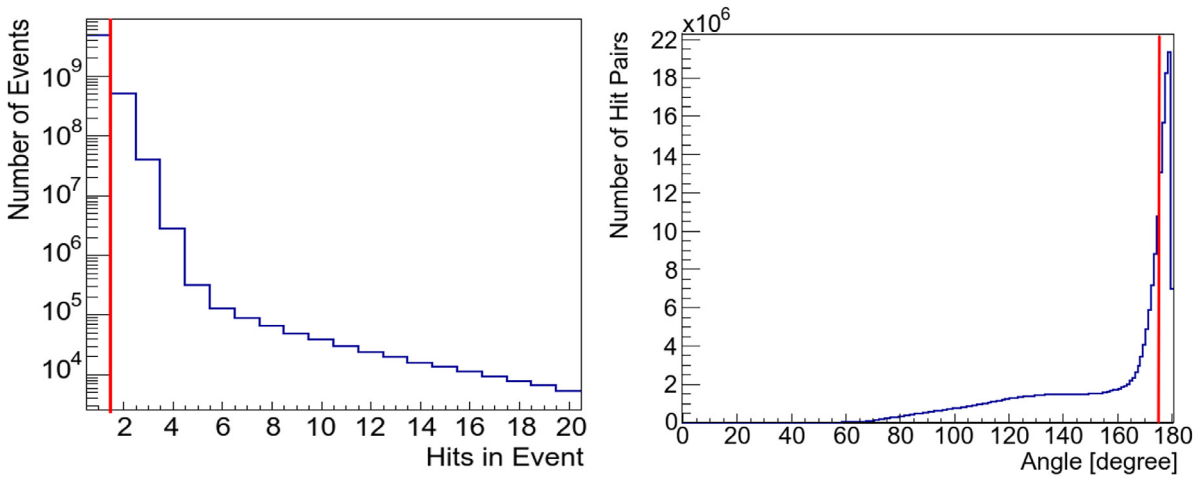

Fig. 23. Selection of back-to-back 511 keV photons, coming from the source in the centre of the detector. The left panel shows the multiplicity of hits in a 4-ns coincidence time window – we are selecting events with at least 2 interactions. The right panel presents the opening angle between two vectors constructed from the position of the source to the positions of hits; as we are expecting the exact opposite flight path of the photons; this angle is selected to be alpha > 175 degrees.

at the SiPM matrices on the ends at the same moment, as shown in Fig. 10., and we can estimate the time walk contribution. If we name the signal arrival time as t' and the reconstructed time at threshold as t^{REC}, we can write:

$$t^{REC} = t' + \alpha/TOT_{SIG}, \quad (13)$$

where TOT_{SIG} is a TOT of the signal, as defined in Equation 1, and α is the time-walk parameter. The signals are registered on the opposite sides of strips A and B, and their time difference equals:

$$\Delta t_{AB} = t_B - t'_A = t^{REC}_B - \alpha/TOT_B - (t^{REC}_A - \alpha/TOT_A) \quad (14)$$

If signals travel the same distance from the centre of the strip their time difference is close to zero, so we can write the following:

$$t^{REC}_B - t^{REC}_A \approx \alpha(1/TOT_B - 1/TOT_A) \quad (15)$$

We name $(1/TOT_B - 1/TOT_A)$ as TOT_{REV} and plot this value against an A–B time difference to visualise the time walk effect, as shown in Fig. 22. After the calculation of the parameter α, we apply the correction to the time t^{REC} of the signal at the SiPM matrix in the following way:

$$t' = t^{REC} - \alpha/TOT_{SIG} \quad (16)$$

where TOT_{SIG} is either TOT_A or TOT_B, depending on which side it was registered.

The method is repeated several times to reduce the effect as much as possible; after each iteration the constant is added to the previous value $\alpha = \alpha_0 + \alpha_1 + \ldots \alpha_n$. This application is evaluated based on the improvement of the TOF resolution, which is described in the next section.

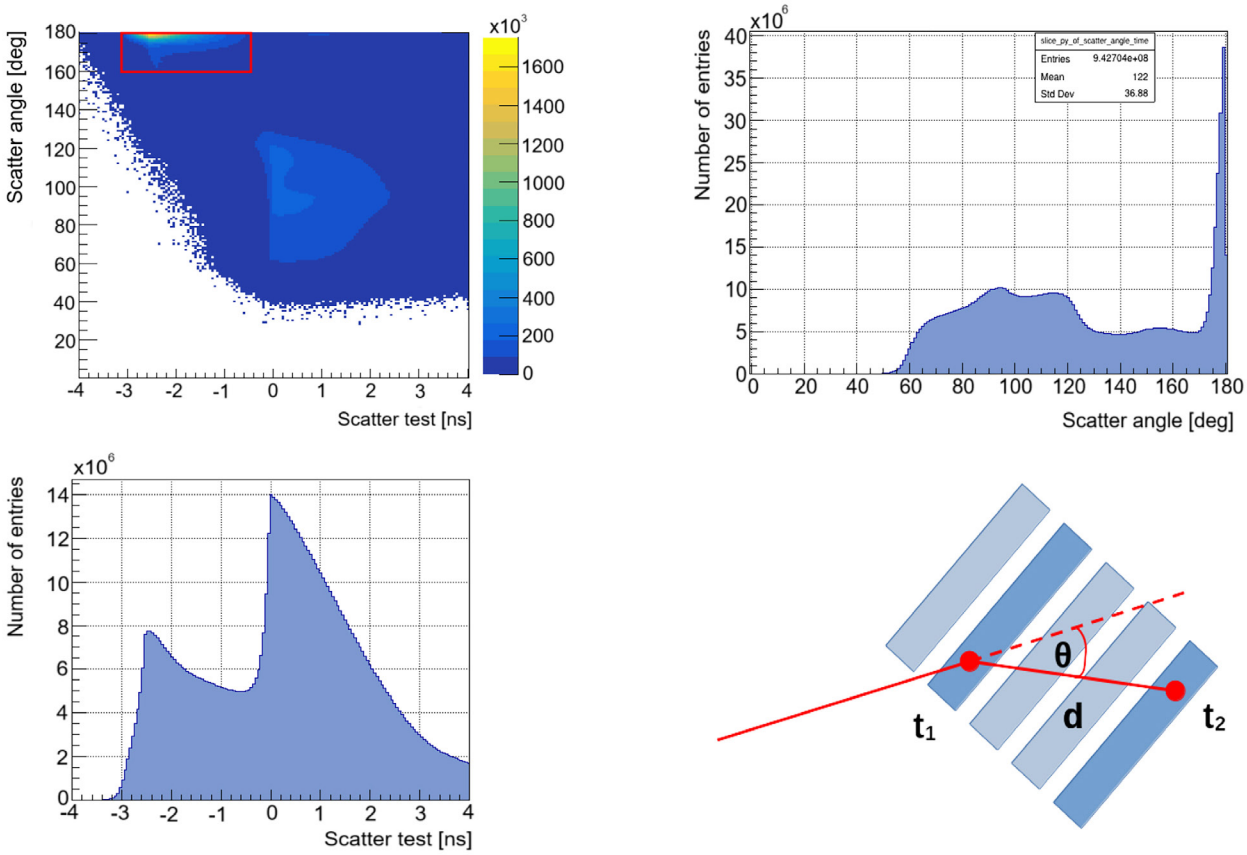

Fig. 24. Reduction of in-detector scatterings in the process of selecting back-to-back 511 keV photons. The lower right panel shows the variables used to draw the histogram in the upper left panel, which shows the dependence of the scatter test measure (x-axis) and the θ angle (y-axis). The upper right and lower left panels are projections of the 2-D histogram. The data contained in the red rectangle is then selected for further analysis, and it is visible that events in this region are separated from the in-detector scatterings, with δ_{sc} around 0 and θ from 60 to 135 degrees.

SELECTION OF ANNIHILATION EVENTS

This section describes the procedure of selecting back-to-back 511 keV photons. For the purpose of this study we apply all the calibrations described in the previous sections.

Data selection

The data sample was prepared in the following way:

1. Selection of events with at least 2 hits in a 4-ns coincidence time window.
2. TOT cut for annihilation Compton edge – selection as shown in Fig. 17., right panel, red lines.
3. Opening angle between the flight vectors (registration point – source position); larger than 175 degrees was chosen.
4. Failed scatter test – the time difference and distance between the combination of every hit in the event indicate that it is not a case of Compton scattering in the detector.

Criteria 1 and 3 are described and illustrated in Fig. 23., and the details of the scatter test are described in the next section.

Scatter test

When it comes to image reconstruction of medical studies, we refer to scatter corrections as a necessary operation that fixes lines of response, because 511 keV photons can interact with the body of a patient or a phantom and be scattered into other directions, departing from their flight path. Here, we will refer to scatterings as the registration of a secondary photon that resulted from an interaction of a primary photon from the source along with any element of the detector. This type of event involves considerable background in the measurement of the modular J-PET prototype, because the strips, which can detect secondary photons, are placed closely together. For every pair of registered photon interactions we test the hypothesis that the latter in time has scattered from the former. The usage of 3 variables, time difference, distance and scatter angle allows us to detect in-detector scattering, pair photons correctly and construct the line of response: time difference, distance and scatter angle. The first two are used to calculate the scatter test measure:

$$\delta_{sc} = \Delta t - d/c \quad (17)$$

where Δt is the time difference of the hits (latter – former), *d* is the distance between the reconstructed positions of the photon

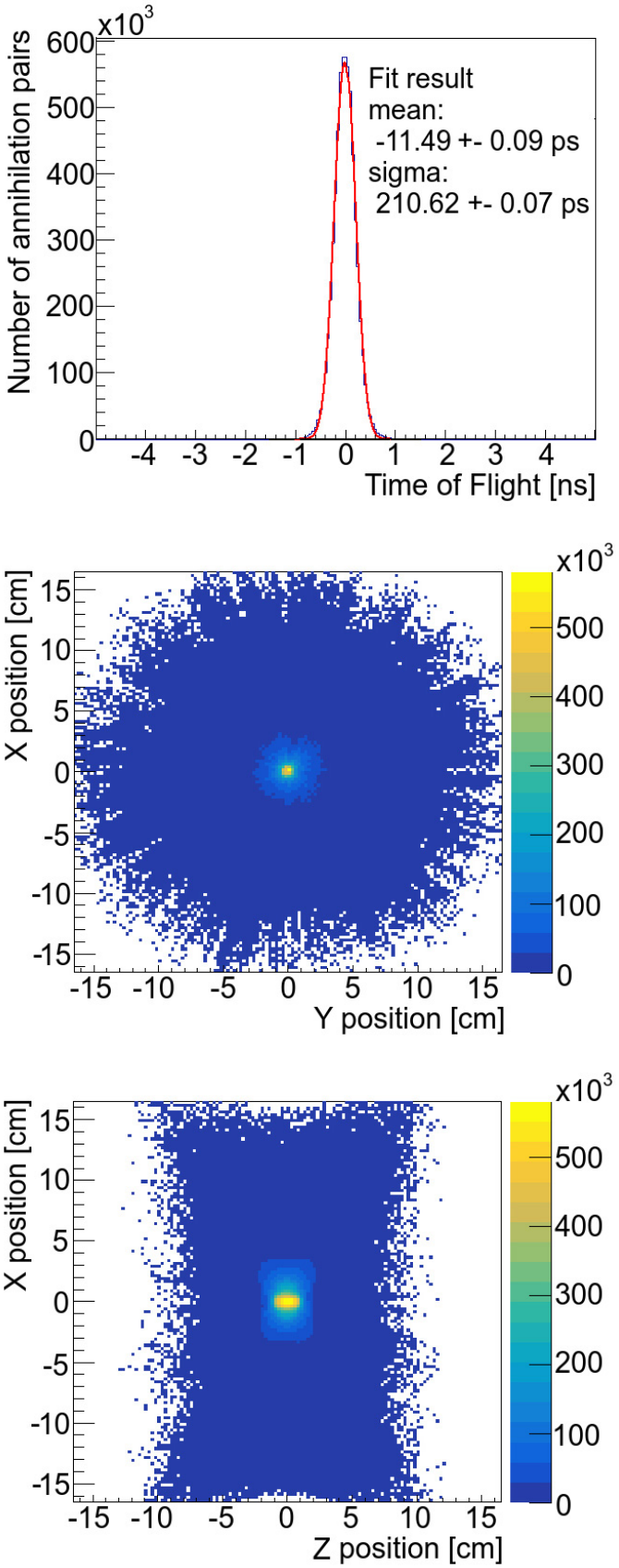

Fig. 25. The upper histogram presents a distribution of the TOF of all the selected pairs registered in the detector. TOF-LOR images of the source are shown on the panels: XY (middle) and ZX (bottom).

interactions, and c is the speed of light. In the case of scattered photons this difference should be around 0, as the particle travels distance d in time Δt. The scatter angle θ is an angle between two vectors: the first – point (0,0,0) and p_1 of the first interaction, the second – interaction points p_1 and p_2. The scatter angle θ is shown in Fig. 24., lower right panel.

RESULTS

The selected pairs of photons are used to make a TOF-LOR image (Fig. 25.) of the source and calculate the TOF distribution, as defined in section *TOF synchronisation*, Equation 11. The TOF distribution is then fitted with a Gaussian curve, and the acquired fit parameter full width at half maximum (FWHM) is calculated, which can also be treated as coincidence resolving time (CRT) for a Gaussian distribution. This relation is given by:

$$\mathrm{FWHM} = 2\sqrt{(2\ln 2)} \cdot \sigma \tag{18}$$

After the selection of all the pairs of hits in the detector the TOF was calculated for each, and the result of the fit parameter was σ = 210 ps, which, according to Equation 18, results in FWHM ≈ 490 ps. The two selected hits, with reconstructed positions $\vec{p_1}$ and $\vec{p_2}$, create a line of response. The annihilation point a is found as a shift along the LOR from its centre:

$$\vec{a} = 0.5 \cdot (\vec{p_1} + \vec{p_2}) + \frac{c \cdot TOF}{2} \frac{\vec{p_2} - \vec{p_1}}{\|\vec{p_2} - \vec{p_1}\|} \tag{19}$$

DISCUSSION

In-detector scatterings

One of the main sources of background in selection of data sample for imaging are the in-detector scatterings, as described in section Scatter test. The simple 3-parameter selection method was introduced. Further studies that would include more sophisticated classification algorithms using, i.e., multilayered perceptrons or boosted decision trees, supported by Monte Carlo simulations, can be performed. Separate MC projects are being developed for J-PET detectors, one based on the Geant4 simulation package, the other on GATE.

Data storage and processing

One of the challenges of processing the data acquired with J-PET is the size of all the files. For the calibration of the detector we gathered 1.2 TB data with a sodium source and 700 GB with the scandium source. The analysis takes a considerable amount of time, especially because it needs to be iterated for some steps. Currently, the workflow takes 72 hours of computing time on a machine with 256 AMD 64-Core, 2.8 GHz processors.

Frequency of calibrations

The frequent detector calibration is not necessary if it is maintained in stable environmental conditions. As shown, it is possible to recalibrate TOT and timing offsets based on the existing files, so the entire process is cut in time. In past years the modular prototype of J-PET was calibrated each time after the change of location or when major issues appeared, e.g., power outage in the laboratory. Future medical protocols should include the estimation of the frequency with which calibrations should be repeated. The current functioning procedures and software contribute to the control of the state of the detector and its synchronisation, offering the chance of achieving the best quality images possible with a J-PET prototype. The separate project aims to provide set of online monitoring tools that are used to detect any issues during the measurements and maintain data quality assurance.

Time walk effect for each SiPM

The method for time walk correction is presented for averaged signals registered by matrices of 4 SiPMs. The calculation of these corrections for each SiPM separately is feasible but would require four times more data acquired with the collimated source, causing all the calibration measurements to last several days. This is a limitation of the method caused by the design of the DAQ system.

NEMA standards

In section *Results* we presented the result of data selection, image reconstruction of the point-like source and the TOF resolution estimation. However, this TOF FWHM value cannot be compared with other total body PET (TB-PET) devices cited in the references, because we did not follow the NEMA NU 2-2018 standards for measurement preparation and data analysis. The estimated number applies only to a source positioned in the centre of the detector.

CONCLUSIONS

We have demonstrated methods to calibrate the J-PET modular detector, which includes step-by-step timing synchronisation and relative normalisation of TOT values. An example of data selection and image reconstruction of a point-like source was presented and TOF resolution was assessed. We estimate that the uncertainties originating from the positioning of the point--like source are negligible, if the sample is placed in the centre of the detector with the precision of 1 mm. It was shown that the calibration procedures do not depend on a type of the isotope if it emits prompt gamma of energy larger than 511 keV.

The J-PET modular detector prototype is a fully commissioned device ready for further studies in medical imaging and fundamental physics, with characteristics comparable with other machines currently functioning in the field of TB-J-PET [20]. The development of TB-J-PET utilising the same technologies and analysis procedures as modular J-PET prototype is a promising endeavour, especially taking into account its cost effectiveness.

ACKNOWLEDGEMENTS AND FUNDING

We acknowledge support from the National Science Centre of Poland through grants no. 2021/42/A/ST2/00423 (P.M.), 2021/43/B/ST2/02150 (P.M.), 2022/47/I/NZ7/03112 (E.S.), 2023/50/E/ST2/00574 (S.S.), 2023/50/E/ST9/ 00576 (A.P.), the Ministry of Science and Higher Education through grant no. IAL/SP/596235/2023 (P.M.), European Union within the Horizon Europe Framework Programme (ERC Advanced Grant POSITRONIUM no. 101199807), the SciMat and qLife Priority Research Areas budget under the program Excellence Initiative – Research University at Jagiellonian University (P.M. and E.S.), We also acknowledge Polish high-performance computing infrastructure PLGrid (HPC Center: ACK Cyfronet AGH) for providing computer facilities and support within computational grant no. PLG/2024/017688 and PLG/2025/018762.

DATA AVAILABILITY

The data that support the findings of this study are available from the corresponding author upon request. The analysis software and supplementary materials are also available upon request.

CONFLICT OF INTERESTS

Paweł Moskal holds patents for PET from plastic scintillators and positronium imaging. Other authors declare no competing interests.

REFERENCES

1. Moskal P, Stępień EŁ. Prospects and clinical perspectives of total-body PET imaging using plastic scintillators. PET Clin. 2020 Oct;15(4):439–52. doi: https://doi.org/10.1016/j.cpet.2020.06.009.
2. Moskal P, Kowalski P, Shopa RY, Raczyński L, Baran J, Chug N, et al. Simulating NEMA characteristics of the modular total-body J-PET scanner-an economic total-body PET from plastic scintillators. Phys Med Biol. 2021 Sep 1;66(17):1–19. doi: https://doi.org/10.1088/1361-6560/ac16bd.
3. Vandenberghe S, Moskal P, Karp JS. State of the art in total body PET. EJNMMI Phys. 2020 May 25;7(1):1–33. doi: https://doi.org/10.1186/s40658-020-00290-2.
4. Spencer BA, Berg E, Schmall JP, Omidvari N, Leung EK, Abdelhafez YG, et al. Performance Evaluation of the uEXPLORER Total-Body PET/CT Scanner Based on NEMA NU 2-2018 with Additional Tests to Characterize PET Scanners with a Long Axial Field of View.

J Nucl Med. 2021 Jun 1;62(6):861–70. doi: https://doi.org/10.2967/jnumed.120.250597.

5. Karp JS, Viswanath V, Geagan MJ, Muehllehner G, Pantel AR, Parma MJ, et al. PennPET Explorer: Design and Preliminary Performance of a Whole-Body Imager. J Nucl Med. 2020 Jan;61(1):136–43. doi: https://doi.org/10.2967/jnumed.119.229997.
6. Prenosil GA, Sari H, Fürstner M, Afshar-Oromieh A, Shi K, Rominger A, et al. Performance Characteristics of the Biograph Vision Quadra PET/CT System with a Long Axial Field of View Using the NEMA NU 2-2018 Standard. J Nucl Med. 2022 Mar;63(3):476–84. doi: https://doi.org/10.2967/jnumed.121.261972.
7. Li G, Ma W, Li X, Yang W, Quan Z, Ma T, et al. Performance Evaluation of the uMI Panorama PET/CT System in Accordance with the National Electrical Manufacturers Association NU 2-2018 Standard. J Nucl Med. 2024 Apr 1;65(4):652–8. doi: https://doi.org/10.2967/jnumed.123.265929.
8. Moskal P, Stępień E, Khreptak A. A vision to increase the availability of PET diagnostics in low- and medium-income countries by combining a low-cost modular J-PET tomograph with the 44Ti/44Sc generator. Bio--Algorithms and Med-Systems. 2024;20(Special Issue):55–62. https://doi.org/10.5604/01.3001.0054.9273.
9. Baran J, Borys D, Brzeziński K, Gajewski J, Silarski M, Chug N, et al. Feasibility of the J-PET to monitor range of therapeutic proton beams. Phys. Med. 2024;118:1–9. doi: https://doi.org/10.1016/j.ejmp.2024.103301.
10. Moskal P, Baran J, Bass S, Choiński J, Chug N, Curceanu C, et al. Positronium image of the human brain in vivo. Sci Adv. 2024 Sep 13;10(37):1–14. doi: https://doi.org/10.1126/sciadv.adp2840.
11. Das M, Bayerlein R, Sharma S, Parzych S, Niedźwiecki S, Badawi R, et al. Development of correction techniques for the J-PET scanner. Bio--Algorithms and Med-Systems. 2024;20(1):101–10. doi: https://doi.org/10.5604/01.3001.0054.9362.
12. Moskal P. Positronium Imaging. In: 2019 IEEE Nuclear Science Symposium and Medical Imaging Conference (NSS/MIC); 26 Oct–2 Nov 2019; Manchester, United Kingdom. IEEE; 2019, p. 1–3. doi: https://doi.org/10.1109/NSS/MIC42101.2019.9059856.
13. Moskal P, Bilewicz A, Das M, Huang B, Khreptak A, Parzych S, et al. Positronium Imaging: History, Current Status, and Future Perspectives IEEE Trans. Radiat. Plasma Med. Sci. 2025;9(8):981–1001. doi: https://doi.org/10.1109/TRPMS.2025.3583554.
14. Moskal P, Kumar D, Sharma S, Beyene EY, Chug N, Coussat A, et al. Nonmaximal entanglement of photons from positron-electron annihilation demonstrated using a plastic PET scanner. Sci Adv. 2025 May 2;11(18):1–10. doi: https://doi.org/10.1126/sciadv.ads3046.
15. Moskal P, Krawczyk N, Hiesmayr BC, Bała M, Curceanu C, Czerwiński E, et al. Feasibility studies of the polarization of photons beyond the optical wavelength regime with the J-PET detector. Eur Phys J C Part Fields. 2018;78(11):1–9. doi: https://doi.org/10.1140/epjc/s10052-018-6461-1.
16. Moskal P, Gajos A, Mohammed M, Chhokar J, Chug N, Curceanu C, et al. Testing CPT symmetry in ortho-positronium decays with positronium annihilation tomography. Nat. Commun. 2021;12: 1–9.
17. Moskal P, Czerwiński E, Raj J, Bass SD, Beyene EY, Chug N, et al. Discrete symmetries tested at 10–4 precision using linear polarization of photons from positronium annihilations. Nat. Commun. 2024;15: 1–10. doi: https://doi.org/10.1038/s41467-023-44340-6.
18. Das M, Sharma S, Beyene EY, Bilewicz A, Choiński J, Chug N, et al. First Positronium Imaging Using 44Sc With the J-PET Scanner: a Case Study on the NEMA-Image Quality Phantom. Trans. Radiat. Plasma Med. Sci. 2026;10(4):593–602. doi: https://doi.org/10.1109/TRPMS.2025.3621554.
19. Ardebili FT, Niedźwiecki S, Moskal P. Evaluation of Modular J-PET sensitivity. Bio-Algorithms and Med-Systems. 2023;19(1):132–8. doi: https://doi.org/10.5604/01.3001.0054.1973.
20. Ardebili TF, Moskal P. Assessing the Spatial Resolution of the Modular J-PET Scanner using the Maximum-Likelihood Expectation-Maximization (MLEM) algorithm. Bio-Algorithms and Med-Systems. 2024;20(Special Issue):1–9. doi: https://doi.org/10.5604/01.3001.0054.8095.
21. Moskal P, Niedźwiecki Sz, Bednarski T, Czerwiński E, Kapłon Ł, Kubicz E, et al.Test of a single module of the J-PET scanner based on plastic scintillators. Nucl. Instrum. Meth. A. 2014 Nov;764:317–21. doi: https://doi.org/10.1016/j.nima.2014.07.052.
22. Kapłon Ł, Baran J, Chug N, Coussat A, Curceanu C, Czerwiński E, et al. Comparative studies of plastic scintillator strips with high technical attenuation length for the total-body J-PET scanner. Nucl Instrum Methods Phys Res Sect A Accel Spectrom Detect Assoc Equip. 2023 Jun;1051:1–10. doi: https://doi.org/10.1016/j.nima.2023.168186.
23. Korcyl G, Alfs D, Bednarski T, Białas P, Czerwiński E, Dulski K, et al. Sampling FEE and Trigger-less DAQ for the J-PET Scanner. Acta Phys. Polon B. 2016;47:491–6. doi: https://doi.org/10.5506/APhysPolB.47.491.
24. Korcyl G, Białas P, Curceanu C, Czerwiński E, Dulski K, Flak B, et al. Evaluation of single-chip, real-time tomographic data processing on FPGA SoC devices. IEEE Trans Med Imaging. 2018 Nov;37(11):2526–35. doi: https://doi.org/10.1109/TMI.2018.2837741.
25. Korcyl G, Moskal P, Beda Teraz?narski T, Białas P, Czerwiński E, Kapłon Ł, et al. Trigger-less and reconfigurable data acquisition system for positron emission tomography. Bio-Algorithms and Med-Systems. 2014;10(1): 37–40. doi: https://doi.org/10.1515/bams-2013-0115.
26. Moskal P, Dulski K, Chug N, Curceanu C, Czerwiński E, Dadgar M, et al. Positronium imaging with the novel multiphoton PET scanner. Sci Adv. 2021 Oct 15;7(42):1–9. doi: https://doi.org/10.1126/sciadv.abh4394.
27. Merlin T, Stute S, Benoit D, Bert J, Carlier T, Comtat C, et al. CASToR: a generic data organization and processing code framework for multi-modal and multi-dimensional tomographic reconstruction. Phys Med Biol. 2018 Sep 10;63(18):185005. doi: https://doi.org/10.1088/1361-6560/aadac1.
28. Agostinelli S, Allison J, Amako K, Apostolakis J, Araujo H, Arce P, et al. GE-ANT4 - A Simulation Toolkit. Nucl. Instrum. Meth. A. 2003;506:250–303. doi: https://doi.org/10.1016/S0168-9002(03)01368-8.
29. Jan S, Santin G, Strul D, Staelens S, Assié K, Autret D, et al. GATE: a simulation toolkit for PET and SPECT. Phys Med Biol. 2004 Oct 7;49(19):4543–61. doi: https://doi.org/10.1088/0031-9155/49/19/007.
30. Choiński J, Jastrzębski J, Kilian K, Mazur I, Napiorkowski PJ, Pękal A, et al. The Radiopharmaceuticals Production and Research Centre at the Heavy Ion Laboratory of the University of Warsaw. Nucl Med Rev. 2012;15(Suppl. C):C5–C8. doi: https://doi.org/10.5603/NMR.2012.0003.
31. Choinski J, Kilian K, Napiorkowski PJ, Pegier M, Sentkowska A, Stolarz A, et al. Radiopharmaceuticals Production and Research Center at Heavy Ion Laboratory of University of Warsaw. Acta Phys. Pol. A. 2021;4(139):413–6. doi: https://doi.org/10.12693/APhysPolA.139.413.
32. www.slcj.uw.edu.pl [Internet]. Stolarz A, Kowalska JA, Jastrzębski J, Choiński J, Sitarz M, Szkliniarz K, et al. Ca targets for Sc production by proton or deuteron irradiation. HIL Annual Report 2016, p. 30 [cited 2025 Dec 10]. Available from: www.slcj.uw.edu.pl/en/reports.
33. Stolarz A, Kowalska JA, Jastrzębski J, Choiński J, Sitarz M, Szkliniarz K, et al. Targets for production of the medical radioisotopes with alpha and proton or deuteron beams. AIP Conf. Proc. 2018;1962:020004. doi: https://doi.org/10.1063/1.5035517.
34. Pałka M, Strzempek P, Korcyl G, Bednarski T, Niedźwiecki Sz, Białas P, et al. Multichannel FPGA based MVT system for high precision time

(20 ps RMS) and charge measurement. J Instrum. 2017 Aug; 12(8):P08001. doi: https://doi.org/10.1088/1748-0221/12/08/P08001.

35. Kamińska D, Gajos A, Czerwiński E, Alfs D, Bednarski T, et al. A feasibility study of ortho-positronium decays measurement with the J-PET scanner based on plastic scintillators. Eur Phys J C Part Fields. 2016;76(8): 1–14. doi: https://doi.org/10.1140/epjc/s10052-016-4294-3.

36. Sharma S, Chhokar J, Curceanu C, Czerwiński E, Dadgar M, Dulski K, et al. Estimating relationship between the time over tiiooioooooohreshold and energy loss by photons in plastic scintillators used in the J-PET scanner. EJNMMI Phys. 2020 Jun 5;7(1):1–15. doi: https://doi.org/10.1186/s40658-020-00306-x.

37. Dulski K, Silarski M, Moskal P. A Method for Time Calibration of PET Systems Using Fixed beta+ Radioactive Source. Acta Phys. Polon. B. 2020;51:195–200. doi: https://doi.org/10.5506/APhysPolB.51.195.